Hindawi
Geofluids
Volume 2019, Article ID 8161469, 20 pages
https://doi.org/10.1155/2019/8161469

Research Article

Fluid Circulations at Structural Intersections through the Toro-Bunyoro Fault System (Albertine Rift, Uganda): A Multidisciplinary Study of a Composite Hydrogeological System

Bastien Walter,[1] **Yves Géraud**,[1] **Yann Hautevelle**,[1] **Marc Diraison**,[1] **and François Raisson**[2]

[1]*GeoRessources, UMR 7359, Université de Lorraine, CNRS, CREGU, ENSG Campus Brabois, 2 Rue du Doyen Roubault, BP10162, F-54505 Vandoeuvre les Nancy, France*
[2]*Total CSTJF, Avenue Larribau, F-64016 Pau Cedex, France*

Correspondence should be addressed to Bastien Walter; bastien.walter@univ-lorraine.fr

Received 8 May 2018; Revised 22 September 2018; Accepted 28 October 2018; Published 27 February 2019

Academic Editor: Domenico Montanari

Regional fault structures along rift basins play a crucial role in focusing fluid circulation in the upper crust. The major Toro-Bunyoro fault system, bounding to the east of the Albertine Rift in western Uganda, hosts local fluid outflow zones within the faulted basement rocks, one of which is the Kibiro geothermal prospect. This major fault system represents a reliable example to investigate the hydrogeological properties of such regional faults, including the local structural setting of the fluid outflow zones. This study investigated five sites, where current (i.e., geothermal springs, hydrocarbon seeps) and fossil (i.e., carbonate veins) fluid circulation is recognized. This work used a multidisciplinary approach (structural interpretation of remote sensing images, field work, and geochemistry) to determine the role of the different macroscale structural features that may control each studied fluid outflow zones, as well as the nature and the source of the different fluids. The local macroscale structural setting of each of these sites systematically corresponds to the intersection between the main Toro-Bunyoro fault system and subsidiary oblique structures. Inputs from three types of fluid reservoirs are recognized within this fault-hosted hydrogeological system, with "external basin fluids" (i.e., meteoric waters), "internal basin fluids" (i.e., hydrocarbons and sediment formation waters), and deep-seated crustal fluids. This study therefore documents the complexity of a composite hydrogeological system hosted by a major rift-bounding fault system. Structural intersections act as local relative permeable areas, in which significant economic amounts of fluids preferentially converge and show surface manifestations. The rift-bounding Toro-Bunyoro fault system represents a discontinuous barrier for fluids where intersections with subsidiary oblique structures control preferential outflow zones and channel fluid transfers from the rift shoulder to the basin, and vice versa. Finally, this work contributes to the recognition of structural intersections as prime targets for exploration of fault-controlled geothermal systems.

1. Introduction

Large varieties of potentially geothermal systems are nowadays recognized, depending on their geological, hydrogeological, and heat source and transfer characteristics (e.g. [1–7]). Current technology development thus broadens the geothermal play types that can be operated, especially in intracratonic area [8]. In order to catalog the geological controls on geothermal resources, Moeck [9] proposed a new geologically based classification, involving both magmatic vs. nonmagmatic and convective vs. conductive dominated geothermal systems. Classification of the different geothermal play types can therefore significantly help in the choice of exploration methods and heat and power production techniques subsequently.

Among the different geothermal play types defined by Moeck [9], geothermal systems are broadly prospected especially in "extensional domain play type (CV3)." This geothermal play type consists in nonmagmatic convection-dominated domains, where active faulting represents

pathways for fluid flow and is responsible for regional high heat flow associated to crustal tectonic thinning (e.g., [10, 11]). This geothermal play type represents a significant part of the worldwide geothermal potential, with many prime examples (e.g., Eastern African Rift System (EARS), European Cenozoic Rift System, and Great Basin Region in USA) (e.g., [12–14]). These fault-controlled plays necessitate a particularly good understanding of the hydrogeological behavior of the structural features and the identification of favorable structural settings. Such identification is critical for extensional basins where geothermal resources may have little or no surface manifestations [15–17]. On the basis of surface geothermal emission locations relative to recurring fault patterns, several authors proposed a general catalog and a ranking of the most favorable structural settings for geothermal activity (e.g., [18–21]). This cataloging approach aims at defining exploration guides for potential evaluation of known resources and discovery of unknown subsurface systems. Despite this, development of geothermal systems needs determination where fluid migration specifically occurs in fault-controlled plays. Unfortunately, examples of field geothermal exploration of fault-controlled systems are poorly represented.

The western branch of the EARS (western Uganda), along which several significant geothermal surface manifestations are now investigated (e.g., Kibiro, Buranga, and Katwe) [22] is an ideal place to study a fault-controlled geothermal play and to develop a play-type-specific field reconnaissance as part of the early stage exploration. This study was carried out along the Lake Albert eastern shore near the Kibiro main hydrothermal site (Figure 1). Several current and fossil fluid circulation zones were identified within the faulted basement rocks of the rift. This work used a multidisciplinary approach (structural geology, geochemistry, and petrology) to investigate (1) the local structural setting of each studied fluid outflow zones and (2) the nature and the source of these fluids. Field work and detailed analyses of fluid circulation features sampled within fractures and breccias of fault rocks, including hydrocarbon materials and carbonate veins, were performed. As the Kibiro geothermal prospect has been already studied, literature data from this site was also synthetized and integrated here. This study contributes to the recognition of generic favorable structural settings of fault-controlled geothermal prospects. Finally, this work also provides new datasets from a scarcely documented area, where fault-controlled fluid recharge and discharge are poorly understood, and provides insights on the hydrogeological behavior of this regional-scale fault system.

2. Geological Setting

In western Uganda, the Albertine Rift System (ARS) forms the northernmost segment of the western branch of the EARS. It extends from the Virunga volcanic province and the Lake Edward in the south to the northern end of Lake Albert within Precambrian magmatic and metamorphic basement rocks. The ARS development was controlled by the regional Precambrian NE-trending structural inheritance and rock fabric [12, 23, 24]. This complex graben system is made up of a series of intracontinental normal fault-bounded basins, each of about ~60–100 km in length and several km in depth, and segmented by transfer faults [25]. The ARS is one of the major hydrocarbon and hydrothermal prospective regions of Eastern Africa, representing an exploration area over 400 km in length and of about 60 km in average width (e.g., [22, 26, 27]).

The Lake Albert basin shows the unique configuration in the western branch of the EARS of a full-graben, bounded by two major antithetic NE-trending fault systems [28]. The eastern flank of this basin is bounded by the Toro-Bunyoro fault system (TBFS) (Figure 1). This fault system was developed through Precambrian basement rocks mainly consisting in different granitoid rock units [29, 30]. Different high-grade banded metamorphic gneisses to granulitic gneisses with variable compositions (granite, tonalite-trondhjemite-granodiorite suite) are recognized in this area. The felsic granulite of the Karuma Complex was dated around 2991 ± 9 Ma [30], while similar TTG gneiss found further south in the foothills of the Rwenzori Mountains were dated by U-Pb age determinations of zircon cores at 2584 ± 18 Ma, 2637 ± 16 Ma, and 2611 ± 14 Ma [31]. The major TBFS is mainly composed of two ~100 km long steeply NW-dipping NE-trending faults connected by the ENE-trending Kaiso transfer structure (Figure 1). The surface expression of this fault system corresponds to subcontinuous 300–400 m high escarpment bordering the lake. Along the fault scarp, only the footwall can be reached and studied thanks to several sedimentary platforms emerging from the lake, notably along the main Kaiso-Tonya (KT) platform, whereas the hanging wall is systematically hidden in the basin.

3. Analytical Methods

Detailed structural and microstructural analysis was carried out for each of the selected working sites. Interpretation of satellite images was correlated with field observations to determine the main structural features of each investigated site. Representative deformed basement rock samples, as well as mineralized veins and hydrocarbon fracture fillings, were collected at the different outcrops in order to describe the deformation state and the fluid migration along the TBFS.

Optical and cathodoluminescence (CL) microscopy observations were used to describe the carbonate grains within the mineralized veins. The CL observations were conducted with vacuum of 50 mTorr, a voltage of 12 kV, and current of 0.2 μA. Fluid inclusion (FI) analyses were conducted on doubly polished sections (200–300 μm thick). Microthermometry was explored using a Linkam MSD600 heating-freezing stage, adapted to an Olympus microscope. Analyses were calibrated with melting-point standards at $T > 25^{\circ}$C and natural and synthetic fluid inclusion standards at $T < 0^{\circ}$C. Heating rate was software-monitored to obtain a $\pm 1^{\circ}$C accuracy. Homogenization temperature (T_h) of the FI was measured during heating stages. However, due to their small size, results of the low-temperature microthermometry analyses (freezing stage) were not clearly interpretable. Additionally, in situ SIMS oxygen and carbon isotopic

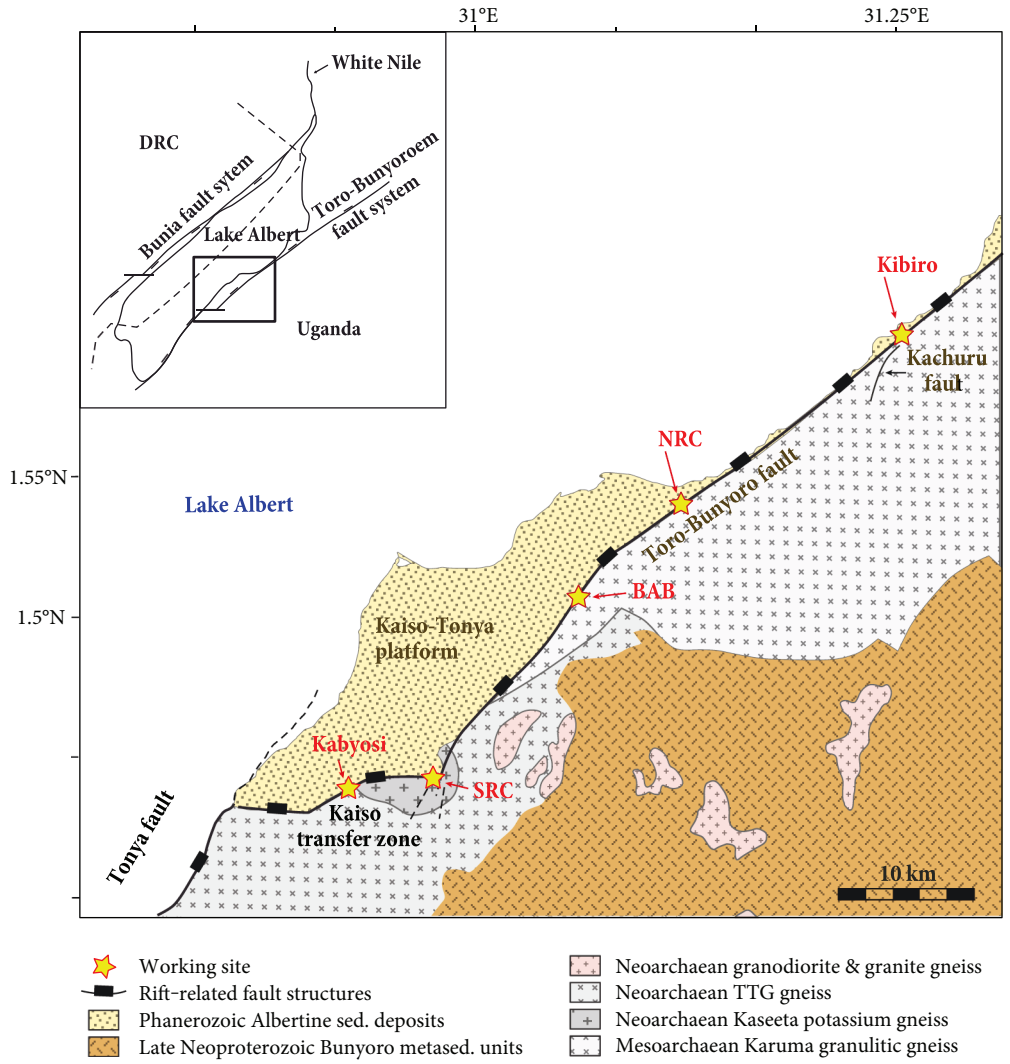

Figure 1: Geological map of the study area and location of the working sites (modified from [29]).

analyses were carried out on carbonate grains from different mineralized veins using a CAMECA IMS 1270 (Cs^+ source) at the CRPG-CNRS laboratory (Nancy, France) following the analytical methods described by Rollion-Bard et al. [32]. Results are expressed using the usual δ notation (‰), with $\delta^{13}C$ and $\delta^{18}O$ values, respectively, relative to the Pee Dee Belemnite (PDB) marine carbonate and Standard Mean Ocean Water (SMOW) reference materials.

Organic geochemistry analyses were performed at the GeoRessources Laboratory (University of Lorraine, France). Asphalt samples were dissolved in dichloromethane in order to recover its soluble fraction. An aliquot of each organic extracts was then diluted into 100 ml of pentane under heating (55°C) and stirring in order to precipitate asphaltene compounds. Asphaltenes were then removed by filtration. The nonasphaltenic fractions (maltenes) were recovered and then fractionated in order to get 3 separate fractions, namely, aliphatic (nonaromatic hydrocarbons), aromatic (aromatic hydrocarbons), and the polar (compounds bearing heteroatoms) fractions. Fractionations were carried out using a Gilson ASPEC instrument and Strata SPE CN cartridges filled up with 1 g of silica gel. The solvents used to recover each fraction were hexane, dichloromethane, and finally a dichloromethane/methanol mixture. These three fractions were analyzed by gas chromatography coupled to mass spectrometry (GC-MS) in order to determine their molecular composition. The GC-MS was a Shimadzu GCMS-QP2010 Plus with a 60 m J&W DB-5 capillary column. The MS operated in the electron impact mode (EI) at 70 eV ionization energy, and mass spectra were scanned from 50 to 500 Da using a quadrupole detector.

4. Geological Characterization of the Studied Sites

This work investigated 5 sites located along the TBFS, where current and fossil fluid migrations were recognized within the faulted basement footwall (Figure 1, Table 1). In order to investigate the role of the different macroscale structural features that may control these fluid circulation zones, a large-scale high-resolution remote sensing digital elevation model (DEM) of the area was used to describe the nearby

Table 1: Working site location and associated fluid circulation marker type.

Site	GPS coordinates	Fluid circulation markers
Kibiro	N1.6737; E31.2557	Current hydrothermal and hydrocarbon seepages
NRC	N1.5650; E31.1175	Fossil hydrothermal veins
Babouns	N1.5095; E31.0572	Fossil hydrothermal veins
SRC	N1.4020; E30.9694	Fossil hydrothermal veins
Kabyosi	N1.3971; E30.9240	Current hydrocarbon seepages

structural lineaments and is presented below. In the field, all these sites were found at the foot of the 300–400 m high fault escarpment where heavily fractured or cataclastic basement rocks were observed. For each of these sites, local aerial images and field observations of the various structural and fluid circulation features are also described thereafter. In comparison to the other working sites of this study, the Kibiro area is the only one where previous geophysical and geochemical studies were published. These data are synthetized and used to build conceptual geological model.

4.1. DEM Structural Analysis of the TBFS Footwall. A large-scale structural study of the TBFS footwall along the KT platform based on manual picking of lineaments from DEM interpretation in geographic information system (GIS) was carried out (Figure 2). Lineament picking and statistical analysis of fracturing of the TBFS footwall was limited landward to a ~5 km wide band from the main fault scarp. High-resolution picking of structural lineaments was performed on a LIDAR 1 m composite DEM image at a sampling scale of 1/50000. In this study, a lineament was considered to be a linear element with a unique length and direction. In order to focus this analysis on the structural features of the TBFS footwall, the main trace of the TBFS (in orange in Figure 2) was not taken into account into the following statistical analysis. 255 lineaments were picked on the analyzed surface. Lineament orientations are represented in a length-weighted rose diagram in Figure 2.

The DEM structural analysis reveals two main NNW- and NNE-striking lineament sets, many of which intersect the main TBFS especially nearby the 5 working sites (Figure 2). A secondary ENE-striking set is also observed, corresponding to lineaments mostly developed along the ENE-trending Kaiso transfer structure. A minor ESE-striking lineament set is additionally recognized in this area. A dense network of oblique structural features therefore affects the TBFS footwall, with a large number of lineaments intersecting the main fault scarp.

4.2. The Kibiro Site. The Kibiro site is located ~20 km northeast of the KT platform, situated on a fan delta of about 0.5×1.5 km along the NE-trending TBFS scarp (Figure 1). With several active hot springs, Kibiro is the main area where thermal fluid discharges occur along Lake Albert. Over the few past decades, several studies were undertaken on this potential geothermal field and various geological, geophysical, and geochemical results were published [22, 33]. The Kibiro active hydrothermal manifestations consist in a main hot spring area called Mukabiga with a few meter large hot water pool directly located at the base of the fault scarp and the two Mwibanda and Muntere salt gardens associated with hot springs located over ~100 m from the scarp through the sedimentary platform (Figure 3(a)). On the lower slopes of the scarp, at about 500 m SW from the Mukabiga springs, several heavily fractured and brecciated basement outcrops show sulfur-related minerals precipitated in cracks. No rising steam was observed but strong smell and fresh sulfur deposits suggested active H_2S (hydrogen sulphide) leakage. Fillings of biodegraded organic material (asphalt) were also observed and sampled from some of these fractures in order to be analyzed for this study.

The main Mukabiga hot springs are located in the axis of a fault-controlled NNW-trending river incision, which intersects the major NE-trending TBFS scarp (Figure 3(a)). Mawejje et al. [34] presented a mapping study of the active and fossil fluid surface manifestations (e.g., hot springs, gas fumaroles, calcite veins and travertines, and silica veins) within an area of ~10 km around the main Kibiro hot springs. According to this study, fluid flow manifestations along the scarp are more pronounced at intersections with other secondary faults, especially where the fault density is higher. Electric, gravity, and magnetic geophysical surveys undertaken in this area showed that the subsurface geothermal resource can be identified landward along the traces of oblique fault lineaments recognized in the rift shoulder [35].

Several geochemical studies of the hot springs and the surrounding area of the Kibiro geothermal prospect presented different results, consisting in geochemical analyses of rock and water samples, stable isotope ratios, spring flow and gas content measurements, and geothermometry modeling. Water samples from all the hot springs of the three main areas (Mukabiga, Mwibanda, and Muntere, Figure 3(a)) have similar geochemical features. These waters are characterized by neutral pH, Na-Cl-dominated salinity up to 4–5 $g \cdot kg^{-1}$ total dissolved solids, and a gas content dominated by methane [33, 36]. At the main Mukabiga area directly located at the base of the main fault scarp, the flow rate is about 4 $l \cdot s^{-1}$ and the temperature ranges between 57 and 86°C. At Mwibanda and Muntere, located over ca. 100 m from the scarp, flow rates and temperature are about 2.5 $l \cdot s^{-1}$ and undocumented and are from 33 to 72°C and up to 45°C, respectively [33, 37]. Stable isotope compositions of water samples indicate that meteoric water contributes as a major component of the Kibiro hot spring recharge. δ^2H data suggest that this meteoric water is originating from a higher elevation point, which can be represented by the high ground of the Mukhihani-Waisembe Ridge located 20 km southeast of Kibiro. On the other hand, the quite different lake and hot spring water d^2H signatures indicate low interaction between both reservoirs during hydrothermal activities [22]. The isotope composition of sulfur and oxygen in sulfates ($\delta^{34}S_{(SO4)}$, $\delta^{18}O_{(SO4)}$) suggest an interaction with crustal materials related to the water-rock interaction highlighted by the strontium isotopes ($^{87/86}Sr_{H2O}$, $^{87/86}Sr_{Rock}$) of the groundwater and the granitic gneiss basement of this area [22]. Using different isotope- or chemical-based geothermometers and

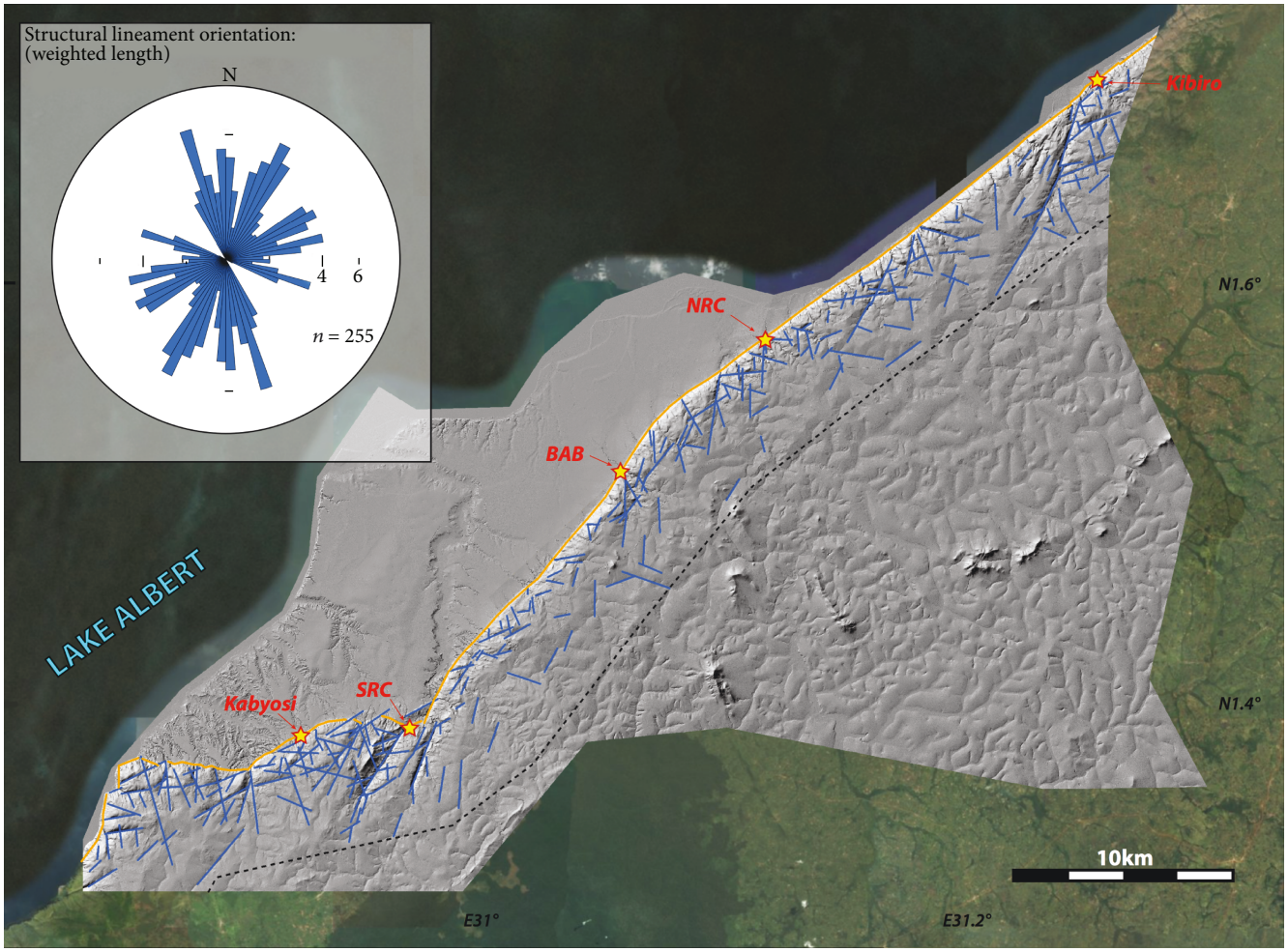

Figure 2: Structural analysis of the TBFS basement footwall on a LIDAR 1 m composite DEM image of the Kaiso-Tonya area.

chemical mixing models (e.g., SiO_2-CO_2), several authors suggest that the Kibiro reservoir has a first subsurface equilibrium temperature of about 200°C. The geothermal fluids have mixed with cold groundwater, producing a second subsurface equilibrium at about 150°C [22, 38, 39]. In conjunction to the geological information, these geochemistry analyses finally suggest that the Kibiro hot springs are most likely associated with an active ~150°C fault-hosted upflow with no direct magmatic heating [33].

4.3. The "North Roadcut" Site. The site called the "North Roadcut" (NRC) is located at the northern end of the KT platform (Figure 1). This winding road cuts the basement footwall of the NE-trending TBFS scarp and exposes the various fractured basement rocks along outcrops up to ~10 m high over a lateral distance of about 200 m (Figure 3(b), Figures 4(a) and 4(b)). Nearby the NRC, N-trending structural lineaments can be recognized with satellite images intersecting the TBFS (Figures 2 and 3(b)). On the field, massive unlithified fault gouge is identified along the northwesternmost part of the NRC, where the major fault structure can be traced, whereas basement with varying densities of fracturing (~10–50 frac·m^{-1}) can be observed further from the base of the scarp. Significant petrographic variations are also observed along this roadcut with ortho- and paraderived gneiss, mica schist, and mafic dykes (Figure 4(b)). Rock samples taken at this site generally contain a complex set of cross-cutting mineralized fractures filled with calcite. The aspect of some of the thicker veins (up to 1–1.5 mm thick) with host-rock microbreccia suggests hydraulic fracturing without kinematic markers. Undeformed millimeter-thick K-feldspar veins are also identified in the various basement rocks of this site (Figures 4(c) and 5(a)). These veins clearly predate the calcite veins observed here.

4.4. The "Baboons" Site. The "Baboons" (BAB) site is located near the central part of the KT platform, where a major incision river cuts the NE-trending TBFS scarp (Figure 1). The

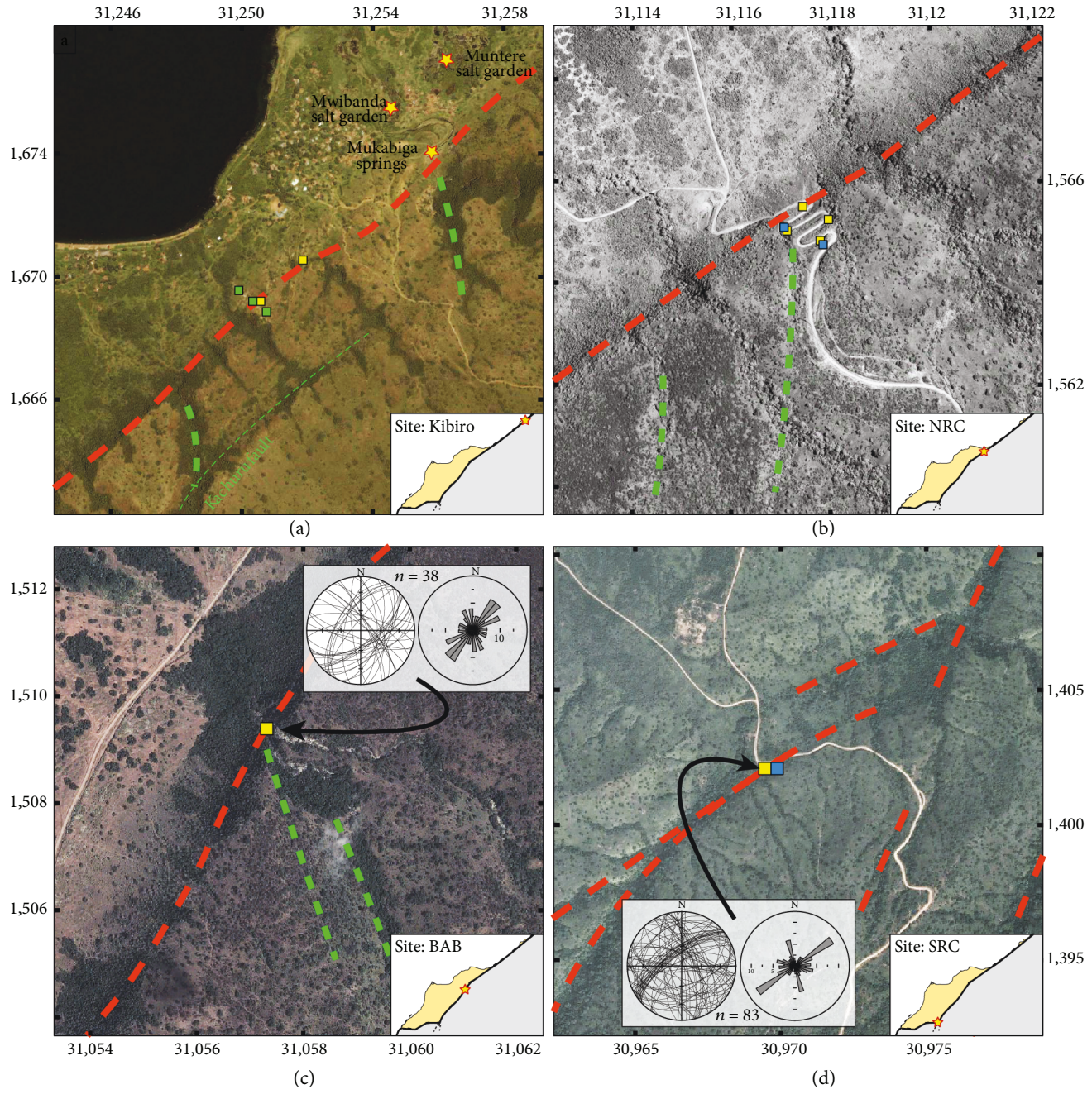

Figure 3: Location maps of the different fluid circulation manifestations identified at the sites (a) Kibirio, (b) NRC, (c) BAB, and (d) SRC. Red dotted lines represent the trace of the TBFS. Stereographic projections (lower hemisphere) and rose diagrams represent carbonate vein orientation measured at sites BAB and SRC, respectively.

last part of this river before flowing down the scarp is controlled by a significant NNW-trending structural lineament intersecting the major rift-bounding normal fault (Figures 3(c) and 4(d)). At the base of the steep fault scarp, the faulted basement appears as rather homogeneous dark grey rocks, with no apparent rock fabric, and consists in cohesive cataclastic rocks (Figure 4(e)). Microstructural observations show that these rocks are composed of a dark micrometric-sized matrix and isolated subangular 10–500 μm fragments of quartz, plagioclase, K-feldspar, and other accessory minerals (Figures 6(a) and 6(b)). Many opaque ultracataclastic bands a few tens of μm thick are also observed. A complex network of fractures and carbonate veins crosscuts these cataclastic rocks (Figure 4(e)). Calcite

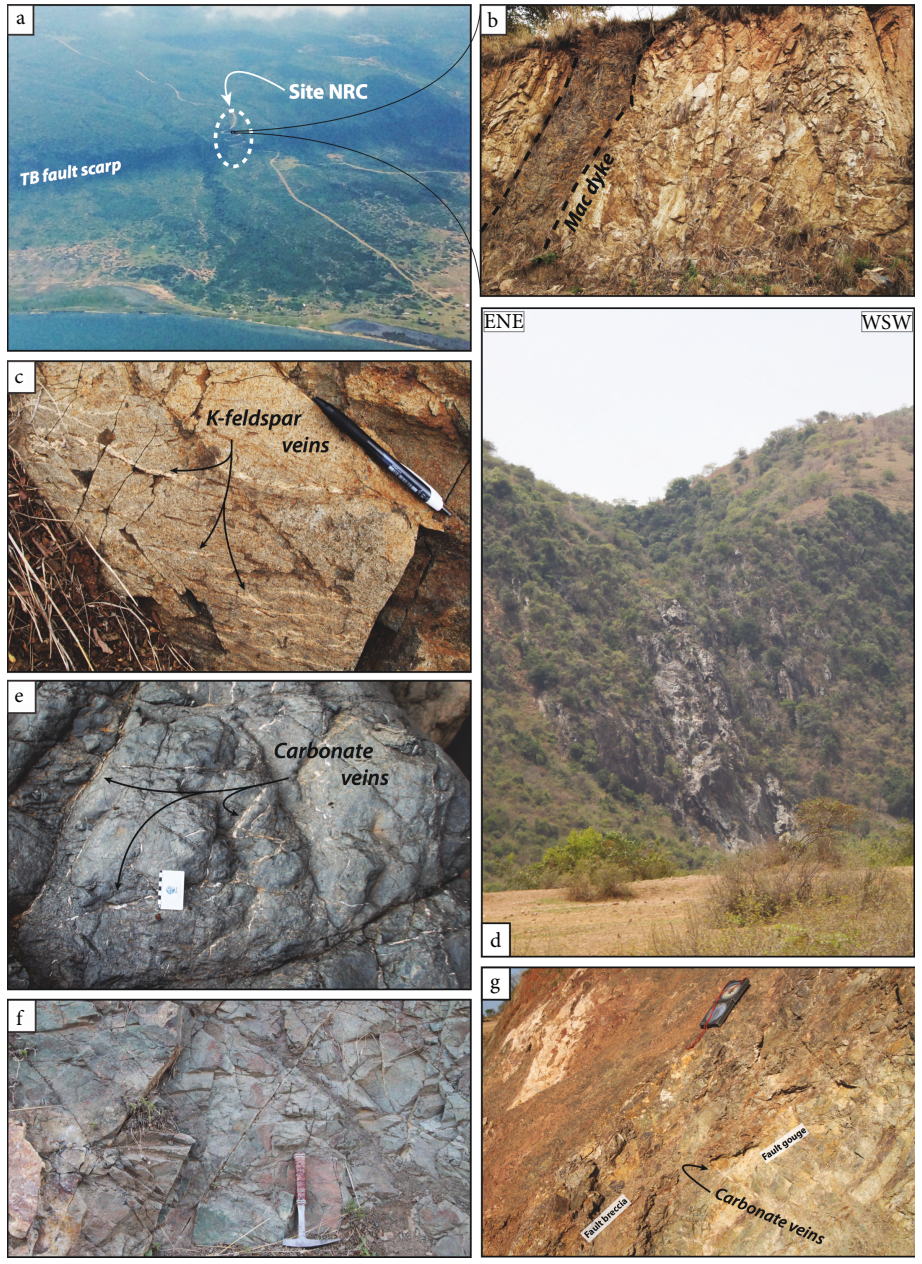

Figure 4: (a) Aerial photograph of site NRC; (b) fractured orthogneiss with mafic dyke intrusion observed at site NRC; (c) multiple K-feldspar veins through gneissic basement at site NRC; (d) long-distance photograph of the fault scarp river incision where site BAB is located; (e) complex network of carbonate veins through the dark cataclastic basement rocks at site BAB; (f) greenish mafic-derived cataclastic rocks overprinted by a dense fracture network observed at site SRC; (g) fault gouge and breccia at site SRC, crosscut by carbonate veins.

veins, up to 1 mm thick, are clearly undeformed and postdate the development of the cataclastic material. Orientation measurements on the field focused on these veins show that the dominant set of these filled fractures follows the NE direction with a high (~70°) NW or SE dip, reflecting the orientation of the TBFS producing the scarp (Figure 3(c)). A secondary set of NNW- to N-striking subvertical veins is also observed, whose orientation is similar to that of NNE-trending structural lineaments intersecting the major rift-bounding fault at this location. E-W oriented calcite veins form also a minor set. Rare K-feldspar veins crosscutting the cataclastic rocks are also observed (Figure 6(b)).

4.5. The "South Roadcut" Site. The "South Roadcut" (SRC) site is located in the relay area between the ENE-trending Kaiso transtensive fault and the NE-trending normal Toro-Bunyoro fault (Figure 1). In this area, this major rift-bounding fault subcontinuous over 100 km long terminates while slightly rotating to NNE trend and splitting into two relatively short subparallel faults about 5 km long (Figure 3(d)). This complex structural accommodation zone consists in a relay ramp about 1 km wide, where the fractured basement is sporadically exposed along the SRC slightly descending to the north-west. The main outcrop is found near the base of the scarp, at the contact between the

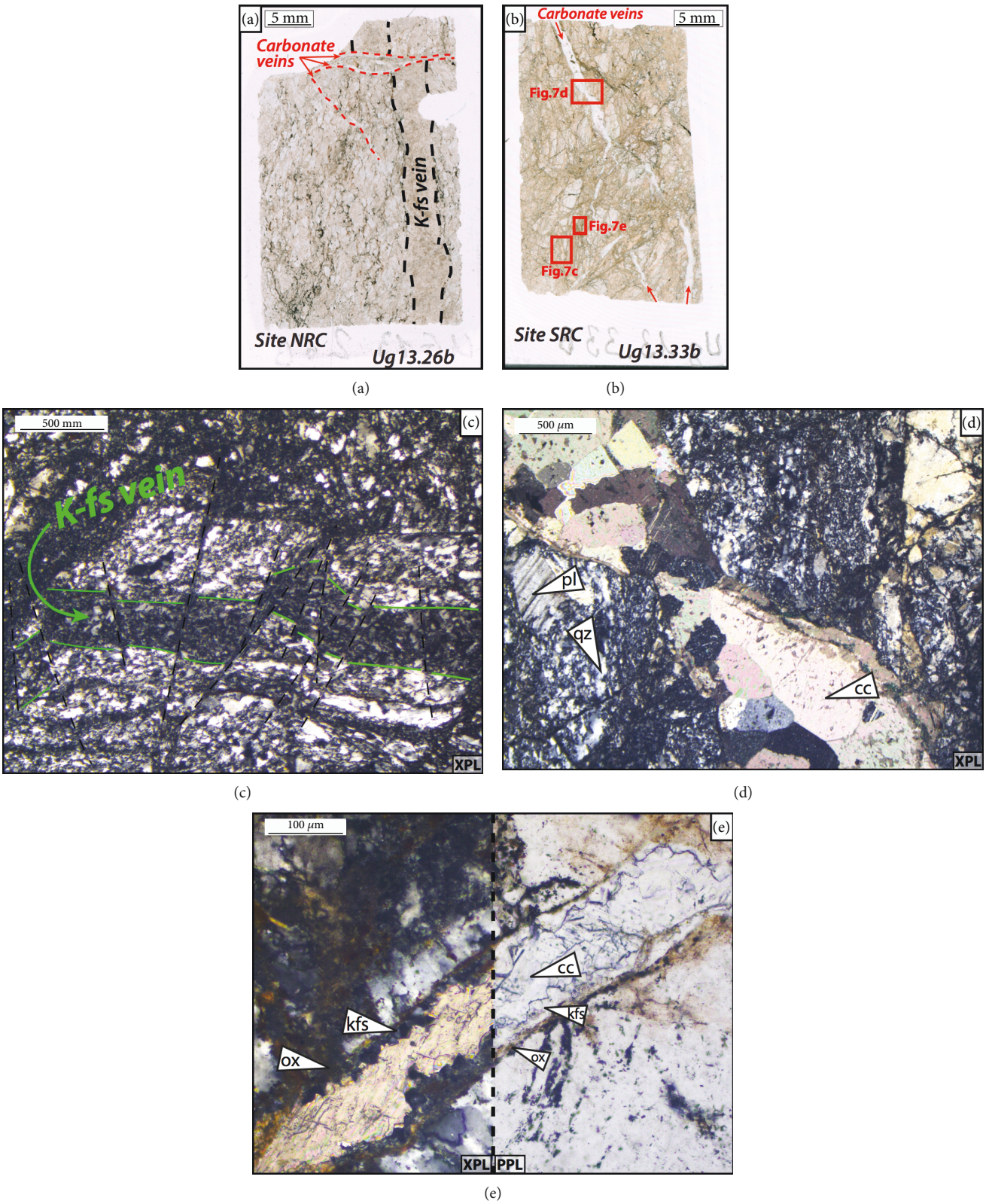

FIGURE 5: (a) Thin-section scan of a gneissic sample from site NRC crosscut successively by K-feldspar and carbonate veins; (b) thin-section scan of a brecciated rock sample from site SRC crosscut by various veins and microphotograph location; (c) highly fractured K-feldspar vein; (d) slightly fractured carbonate vein through the cataclastic rock matrix; (e) undeformed vein with successive K-feldspar (and oxides) and carbonate mineralization. (pl: plagioclase; qz: quartz; cc: carbonate; ox: oxide; kfs: K-feldspar; XPL: cross-polarized light; PPL: plane-polarized light).

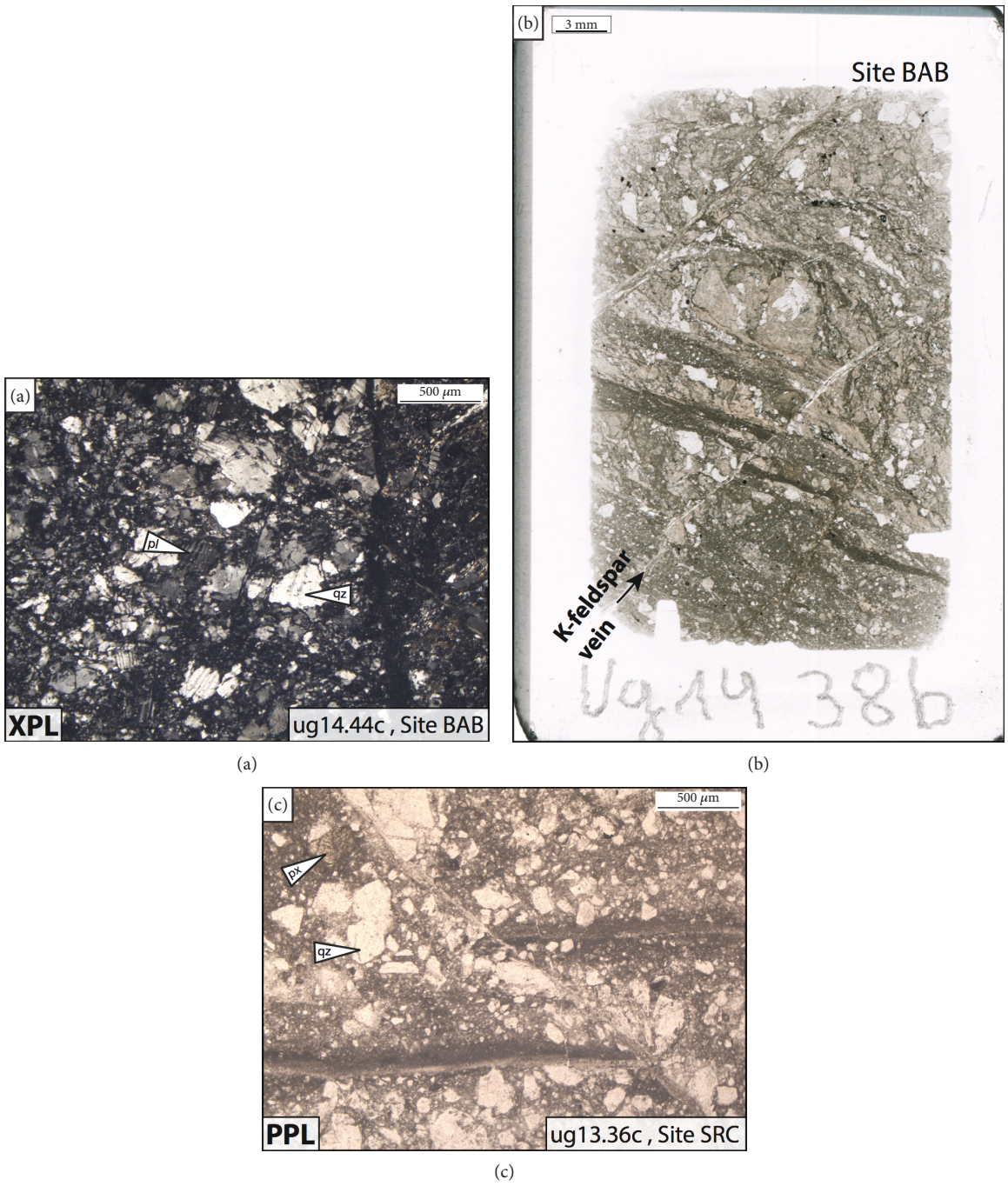

(a) (b) (c)

Figure 6: Microphotographs (a, c) and scan of thin section (b) illustrating the cataclastic deformation observed at sites BAB and SRC (pl: plagioclase; qz: quartz; px: pyroxene; XPL: cross-polarized light; PPL: plane-polarized light).

sedimentary units of the KT platform and the faulted basement of the relay ramp. This large outcrop of ~100 m long and several meters high corresponds to the footwall of the fault. The highly deformed basement of this outcrop is composed of greenish mafic rocks and granitoids with diffuse and unclear contacts (Figures 4(f) and 4(g)). Thin-section observations of the mafic rocks show that cataclasis occurred with the development of dark fine-grained matrix and isolated subangular 10–300 μm fragments of plagioclase, pyroxene, and quartz (Figure 6(c)). Granitoid rocks are generally highly brecciated but do not show such cataclasite texture. A number of K-feldspar veins are heavily deformed by the brecciation process (Figures 5(b) and 5(c)). However, later K-feldspar mineralization appears also to develop after rock breccia, associated with a complex and dense set of crosscutting calcite veins (Figure 4(g), 6(b), and 7(a)). Microstructural observations show that some minor K-feldspar precipitation predates the carbonate deposits, using the same

undeformed veins through the cataclastic rocks (Figures 5(d) and 5(e)). Consequently, all the carbonate veins appear to postdate the high deformation developed by the fault zone, whereas fluid circulation associated to the K-feldspar precipitates seems more diachronous regarding the relative fault zone activity. Some of the thicker calcite veins (up to 2 mm thick) show elongated grains and host-rock microbreccia, suggesting hydraulic fracturing process during development (Figures 7(b) and 7(c)). Along the western part of the outcrop through both mafic and granitoid rocks, the dominant calcite veins follow mainly the NE direction with a high (~70°) NW dip (Figure 3(d)). Other minor subvertical vein sets are also observed with NNW and E-W strikes.

4.6. The Kabyosi Site. The Kabyosi site is located along the ENE-trending Kaiso transfer fault (Figure 1). Several hydrocarbon seepages are located at the base of the scarp and along a fault-controlled river incision (Figure 8(a)). Two main structural lineament sets are observed in the footwall of this complex area, respectively, characterized by ENE trend, parallel to the fault scarp, and by variable NNW to NNE trend. Five oil seeps were identified, systematically located at the intersection between these two lineament sets. Most of the hydrocarbons soak highly fractured and brecciated crystalline basement material (Figures 8(b)–8(d)), and it is still wet and viscous, confirming these fluid circulations to be subcurrent. Except for the northernmost seepage located at the base of the major fault scarp, these faults are ~10–15 m thick with a minimum fracture density of ~30 frac·m^{-1}. These structures are generally characterized by a fault core up to few meters thick, where breccia and fracture densities over 100 frac·m^{-1} are observed, associated with the highest hydrocarbon volumes. Dominant fractures follow mainly the ENE direction with a high (~60–70°) WNW dip, reflecting the Kaiso transfer fault orientation. Minor subvertical fracture sets are also identified with variable NW-SE to NNE-SSW strike (Figure 8(a)).

5. Geochemistry

Different features of current and fossil fluid circulations from the five working sites presented above were investigated to obtain information on their composition and source. Results of hydrocarbon analyses gathered from both Kibiro and Kabyosi sites and petrological and geochemical data of carbonate veins sampled at sites NRC, BAB, and SRC are then presented.

5.1. Molecular Composition of Asphalt Filling from Kibiro and Kabyosi Sites. At the Kibiro and Kabyosi sites, asphalt was found as fracture fillings or part of breccia matrix in basement fault zones. Their molecular composition can provide information on these organic fluids as their origin, in terms of source rocks, and their evolution during their migration throughout the fault zone. Two samples from the Kibiro site and four from the Kabyosi site were analyzed to assess their molecular signature.

These asphalt fillings were mostly soluble in dichloromethane and most of its soluble fraction was mainly composed of asphaltenes, which cannot be precisely characterized. The maltene fraction of these asphalts showed a rather unusual molecular composition with a total absence of characteristic standard components of crude oil like *n*-alkanes and acyclic isoprenoids. Most of the maltene compounds were present in the aliphatic fractions.

Chromatograms of the aliphatic fractions of the Kibiro samples shows the presence of an unresolved complex mixture (UCM) and sulfur as well as hopanoid compounds (Figure 9(a)). Hopanoids are pentacyclic triterpenoids initially present in the cell walls of bacteria and are widely distributed in sedimentary organic matter due to the abundance of bacteria in all environments. Consequently, precise identification of hopanoids can carry many valuable postdepositional information. For instance, in bacteria, hopanoids are present in the biological configuration (17β(H),21β(H)) and are then gradually transformed into a geological configuration (17α(H),21β(H)) via thermal maturation. Identification of these hopanoids is indicated in Figure 9(a) for the Kibiro samples. These hopanoids were composed of C_{27}, C_{29}, and C_{30} hopanes as well as hopenes (unsaturated hopanes). Two of the hopanes presented a biological configuration and no hopane with a geological configuration was detected. Chromatograms of the aliphatic fractions of the Kabyosi samples do not present an unresolved complex mixture as in the Kibiro samples and are also characterized by the presence of hopanoids even if they are different from those of the Kibiro site (Figure 9(b)). These hopanes consist of C_{27}, C_{28}, and C_{29} hopanes while C_{30} hopanes were only present at low contents. For samples of both sites, homohopanes (>C_{30} hopanes) are absent. The large predominance of hopanoids, which are widely synthetized by bacteria together with the lack of acyclic alkanes, which are the first compounds assimilated by microorganisms, suggests that the oil was intensively affected by biodegradation processes after its migration in the faulted basement. This intense biodegradation is moreover attested by the presence of 17α(H),21β(H)-25-norhopane in the Kabyosi samples since this molecular biomarker is typically produced by hydrocarbon-degrading bacteria. Furthermore, hopenes and hopanes presenting the biological configuration (17β(H),21β(H)) disappear during maturation of organic matter. This is why they are systematically present in immature source rocks but never recovered in conventional oils. Therefore, their occurrence should be unlikely in the asphalt fillings at Kibiro and can only be explained by a late bacterial origin. The presence of such hopanoids, which are much more abundant than the other compounds, also supports an intense biodegradation of the initial crude oil. Unfortunately, the original molecular signatures were deeply affected and most of the molecular biomarkers that bear information on the source of the oil were totally consumed by hydrocarbon-degrading bacteria.

In an attempt to recover the initial molecular signatures of these deeply biodegraded asphalt samples, artificial maturations were carried out on the asphaltene fractions of the Kabyosi samples (Figure 9(c)). Despite clear information about the origin of these fluids, regarding the sampling location and the proven oil resources of the Lake Albert, the HC seepages observed in the faulted basement footwall of the

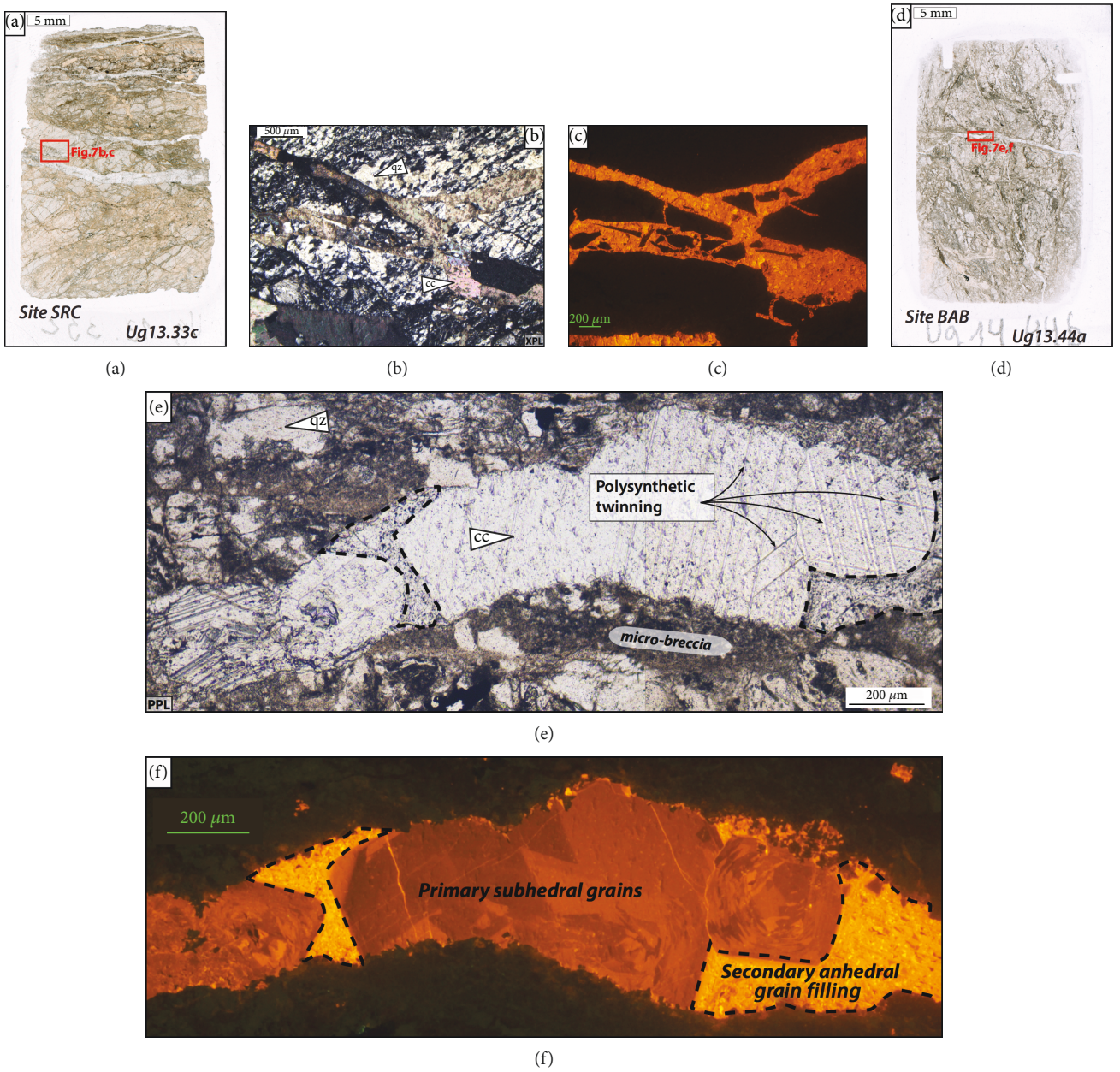

Figure 7: (a) Thin section scan of a brecciated rock sample from site SRC crosscut by undeformed veins and microphotograph location; (b) cross-polarized light and (c) cathodoluminescence microphotographs of a complex carbonate vein network with host-rock microbreccias; (d) thin-section scan of a cataclastic rock sample from site BAB crosscut by undeformed carbonate veins and microphotograph location; (e) plane-polarized light and (f) cathodoluminescence microphotographs of a polyphased carbonate vein with primary twinned subhedral grains and secondary nontwinned anhedral grains. (qz: quartz; cc: carbonate; XPL: cross-polarized light; PPL: plane-polarized light).

TBFS can be assumed to be related to a sedimentary source rock from the ARS basin. Oils are transformed during their transfer by bacterial activity.

5.2. Calcite Vein Analysis. Complex sets of carbonate veins cross-cutting the massive cataclastic rocks of the faulted basement footwall were recognized in the study areas along the major fault scarp (Figures 5, 7). Assuming these cataclasites were formed by the TBFS activation during the ARS evolution since Upper Miocene, the cross-cutting mineralized fractures filled with carbonate are locally postdating the major deformation episodes. Similar carbonate veins were identified in the fractured basement of the Kibiro site near the main active hot springs [34]. These carbonate veins can therefore represent relatively recent fossil fluid circulation zones.

At NRC, BAB, and SRC, the mineralized fractures are generally organized according to several subvertical orientation sets. These orientation sets appear to reflect the local orientations of the fault scarp and macroscale structural lineaments (cf. BAB, SRC sites, Figures 3(c) and 3(d)). No apparent criteria could be observed to identify any relative

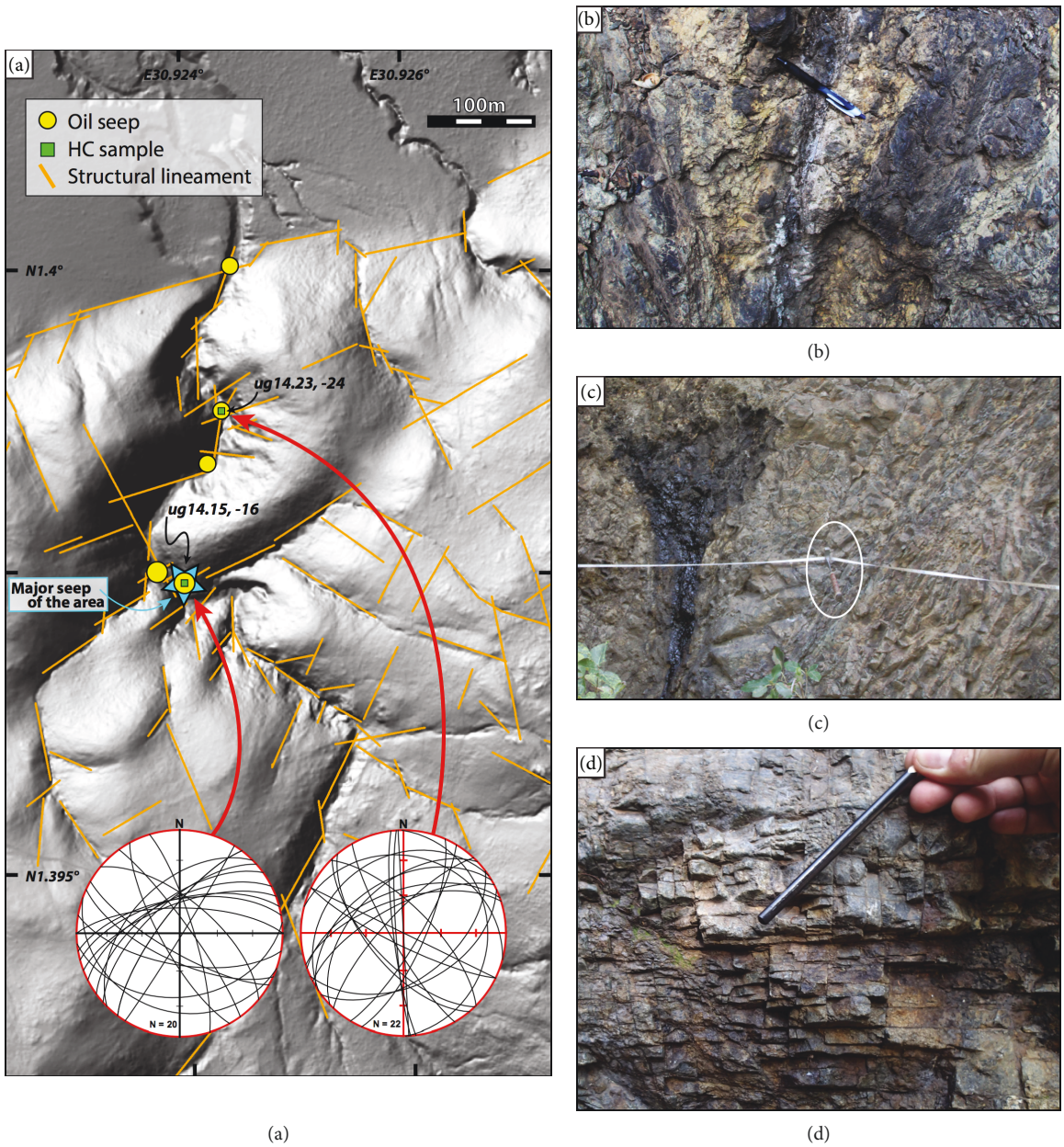

(a) (b) (c) (d)

Figure 8: (a) Hydrocarbon (HC) seeps and sample location map and structural lineament interpretation based on a 1-meter DEM image of the Kabyosi area. Stereographic projections (lower hemisphere) represent fracture orientation measured close by two seeps; photographs illustrating the high brittle deformation associated to the Kabyosi HC seeps; (b) fault gouge and adjacent fractured rocks soaked with HC and sulfur deposits; (c) photograph of the major leakage of the area, occurring in the middle of a ~10 m thick fault zone; (d) dense fracture network near the major seep with isotropic HC flow.

chronology relationship between the different sets. Veins are 0.1 to 1–2 mm thick and show no relationship with orientation. Host-rock hydraulic microbreccias are commonly observed. Under cathodoluminescence (CL), all the carbonate veins are characterized by brown-orange shades, with slight color variations highlighting grain geochemical zonation and growth orientation (Figures 7(c) and 7(f)). Regarding the borders of the veins, no clear grain preferential orientation or elongation can be observed, which could have suggested tensional or shear fractures. Veins with aperture > 200 μm generally show relatively large subhedral carbonate grains and anhedral secondary filling grains (Figures 7(d)–7(f)). Thinner veins are generally composed of subhedral grains and do not show clear polyphasing relationships. In the wider veins, deformation polysynthetic twinning with variable orientations of the subhedral grains is often observed (Figure 7(e)), whereas no twinning is observed in the secondary anhedral filling grains.

Fluid inclusions (FI) were recognized in most of the carbonate veins, with size ranging from ~1 up to 10 μm. Vapor bubbles visible in the largest FI were observed generally moving rapidly at room temperature. No fluorescence of the

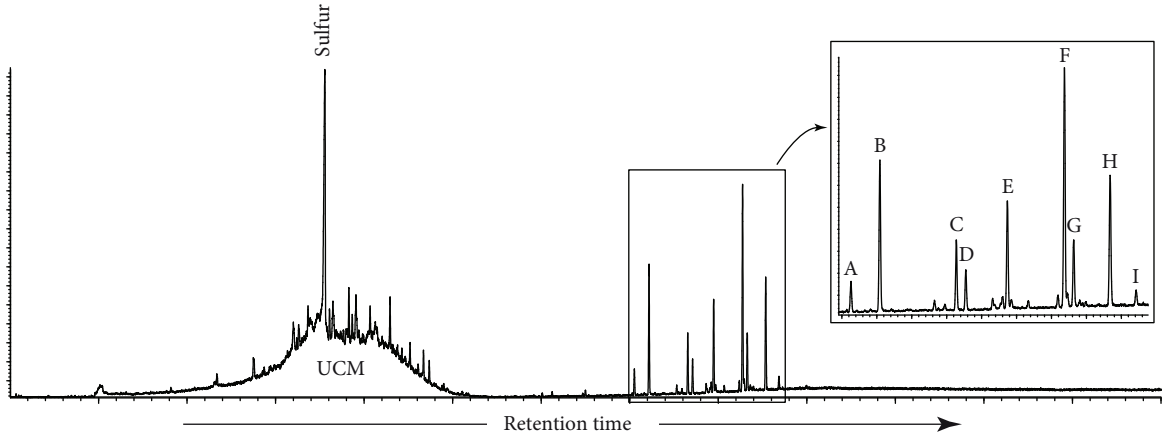

A : 22,29,30-trisnorhop17(21)-ene
B : 17β(H)22,29,30-trisnorhopane
C : hop-17(21)-ene
D : 17β(H),21α(H)-normoretane
E : 17β(H),21β(H)-norhopane
F : C31-homohopene
G : Unidentified compound
H : C31-homohopene

(a) Kibiro site

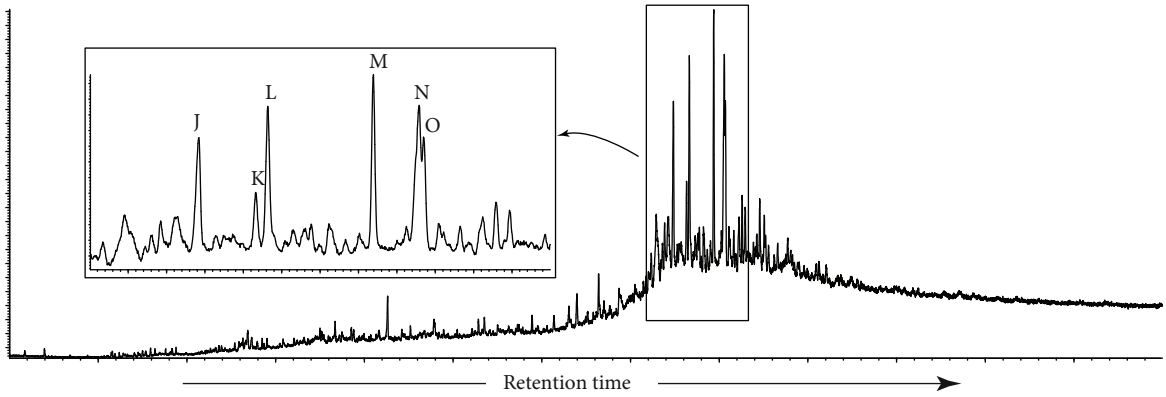

J : 17α(H)-22,29,30-trisnorhopane
K : Trisnorhopane
L : Bisnorhopane
M : 17α(H),21β(H)-25-norhopane
N : 30-norhopane
O : 30-norhopane

(b) Kabyosi site

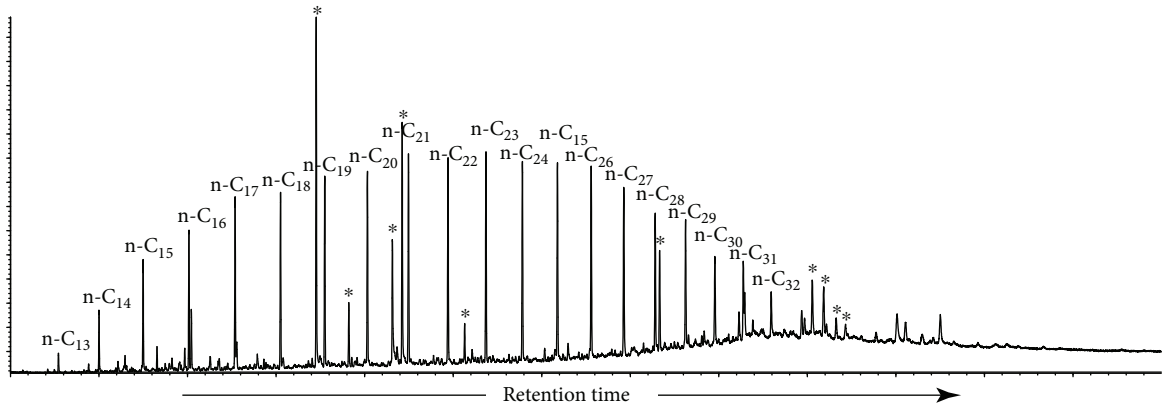

n C_{xx} :*n* - alcanes (xx indicates the number of carbon atoms)
* Contaminants

(c) Artificial maturation products of asphaltenes from the Kabyosi site

Figure 9: (a, b) Gas chromatograms of the aliphatic fractions of the asphalt fillings from the Kibiro and Kabyosi sites, respectively; (c) gas chromatogram of the artificial maturation products of asphaltenes recovered from the Kabyosi asphalt fillings.

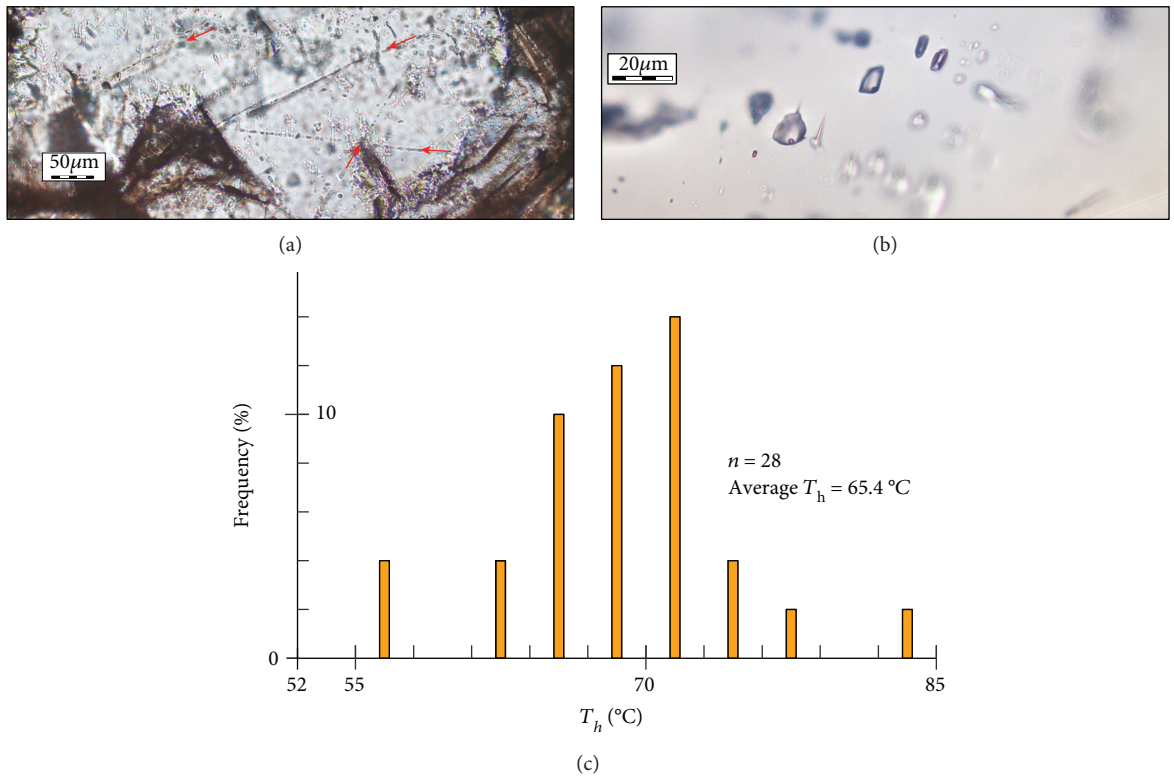

FIGURE 10: Plane-polarized light microphotographs of sample ug13.33 (site SRC) of (a) fluid inclusion secondary trails in large subhedral twinned carbonate grains (indicated with red arrows); (b) irregular-shaped fluid inclusions in a secondary anhedral nontwinned carbonate grain; (c) frequency plot of homogenization temperatures (T_h) of fluid inclusions measured in a sample ug13.33 (site SRC).

liquid phase was observed under ultraviolet (UV) light. FI were found in both twinned and nontwinned carbonate grains. In large subhedral twinned grains, FI are generally observed as secondary trails, where inclusions are elongated according to the trail axes (Figure 10(a)). In secondary anhedral nontwinned grains, FI are generally slightly bigger with irregular morphologies and form assemblages of 2–10 inclusions (Figure 10(b)). Only the thickest carbonate veins from sample ug13.33 (site SRC) were sufficiently large to prepare fragments for FI microthermometry analysis. 28 FI were heated to measure homogenization temperatures (T_h) in both trails within subhedral grains and subisolated assemblages within anhedral secondary grains. T_h values range from 54 to 80°C, with a majority of data lying between 64 and 70°C (Figure 10(c)). Phase transitions during low-temperature microthermometry analysis (freezing stage) were not clearly interpretable.

Oxygen and carbon stable isotope analyses were carried out on carbonate grains in different mineralized fractures from NRC, BAB, and SRC. Results are reported in Figure 11 and Table 2. CL imaging allowed to separate the measurement points between the different grains, in order to average the isotopic ratio data per grain. Both twinned subhedral and nontwinned anhedral grain types were easily recognized on the analyzed veins of sample ug14.44 from BAB (Figures 7(e), 7(f)) and their isotope analysis results are therefore distinct. The isotopic values measured in carbonate veins from sample ug13.16 (NRC) range between 13.7 and 20.7‰ for $\delta^{18}O$ (SMOW) and between 2.6 and 14.8‰ for $\delta^{13}C$ (PDB). Those from sample ug13.33 (SRC) have $\delta^{18}O$ and $\delta^{13}C$ values ranging from 22.9 to 30.2‰ SMOW and from −5.2 to 6.9‰ PDB, respectively. In sample ug14.44 (BAB), large subhedral twinned grains show $\delta^{18}O$ and $\delta^{13}C$ values, respectively, ranging from 16.1 to 19.6‰ SMOW and from 1.0 to 8.1‰ PDB. Values from secondary anhedral filling grains measured in the same veins are different, with $\delta^{18}O$ and $\delta^{13}C$ ranging from 20.1 to 24.3‰ SMOW and from −0.5 to 2.7‰ PDB, respectively.

Oxygen isotopic compositions of the fluids from which the different carbonate veins precipitated were determined using the fractionation curve formula between calcite and water following this expression:

$$10^3 \ln\left(\frac{\delta^{18}O_{cc} + 1000}{\delta^{18}O_{H2O} + 1000}\right) = 4.01\left(\frac{10^6}{T^2}\right) - 4.66\left(\frac{10^3}{T}\right) + 1.71, \quad (1)$$

where $\delta^{18}O_{cc}$ and $\delta^{18}O_{H2O}$ are the oxygen isotopic ratio of the carbonate and the forming fluid, respectively, and T is the precipitation temperature (in Kelvin). Temperature value used in this formula corresponds to the average T_h of 65.4°C measured in sample ug13.33 by FI microthermometry. As no T_h could not be measured because of the small-size FI in the other samples, this average temperature value was also applied to samples ug13.16 and ug14.44 calculation. Using the $\delta^{18}O_{cc}$ values obtained for the analyzed grains in the different veins, oxygen isotopic composition of the fluids

obtained for samples ug13.33 and ug13.16 ranges from −0.27 to 6.88‰ SMOW and −9.50 to −2.46‰ SMOW, respectively (Table 2). Polyphased carbonate veins in sample ug14.44 show different $\delta^{18}O_{H2O}$ values between primary subhedral and secondary anhedral filling grains, varying from −6.97 to −3.52‰ SMOW and −3.05 to 1.12‰ SMOW, respectively.

6. Discussion

The hydrogeological behavior of regional-scale fault zones in rift basins is critical for many practical fluid flow applications. Regarding the Lake Albert basin economic potential for both geothermal and hydrocarbon energies, especially as a prospective fault-controlled "extensional domain play-type (CV3)" geothermal system [9], insights into the hydrogeological system of the eastern rift-bounding TBFS need to be enhanced. From the data of the five different working sites presented in this study, we will discuss hereafter the control of the structural features on this hydrogeological system, as well as the fluid sources that supply it.

6.1. The Transfer Plumbing System. Transfers are constrained by several objects or structures: the NE-trending normal TBFS and associated structures, the fault network, and the relay ramp of Kaiso. All together, they contribute to define the plumbing usable to fluid transfer.

6.1.1. The TBFS. Major faults with thick fault core of clayey-rich gouge or lithified cataclastic material may act as impermeable barrier for fluid flow [40, 41]. Regarding the thick fault core materials observed on the basement footwall of the scarp at each working site and the systematic fault intersection setting identified at the investigated fluid circulation zones, most parts of the TBFS without such passing through structural pattern appear impermeable to fluid flow. In classic models of fault zone architecture, the localized high-strain impermeable fault core is surrounded by a distributed zone of highly connected and dense fractures and faults, corresponding to the relatively permeable damage zone [41, 42]. The transfer properties of the fault core produce a compartmentalization between potential basin fluids and meteoric fluids on the shoulders.

6.1.2. Fracture and Fault Network. Large-scale DEM analysis of the area shows a dense network of oblique lineaments intersecting the TBFS, with a dominant NNW to NNE direction (Figure 2). Locally, the setting of the three northernmost investigated fluid circulation sites consists in the intersection between the NE-trending normal TBFS and N- (cf. site NRC) or NNW-trending (cf. Kibiro, site BAB) structural lineaments identified through the basement footwall (Figures 2 and 3(a)–3(c)).

Considering that the fault core rocks observed along the scarp developed during paroxysmal deformation events during the long-term tectonic evolution since Upper Miocene [12, 28], the fracture networks crosscutting the cataclastic material were active at least once after the fault core cataclasis development and postdate these events. These fracture networks developed at structural intersections through the fault core of the TBFS represent then connected pathways for fluid flow between the damage zones on both sides of the fault structure as developed at Kibiro. They contributed subsequently to produce "x-crossing" fracture networks through the fault core rocks of the TBFS.

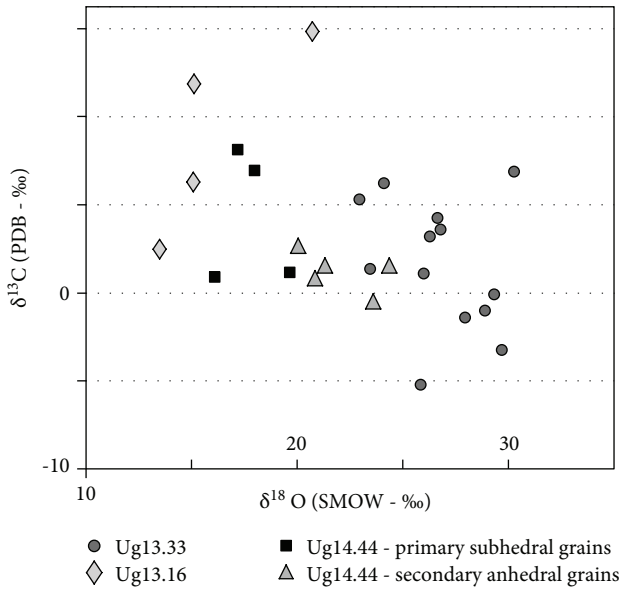

Figure 11: Average isotopic compositions ($\delta^{18}O$ and $\delta^{13}C$, ‰) of different grains measured in carbonate veins from the three working sites SRC (sample ug13.33), NRC (sample ug13.16), and BAB (sample ug14.44, see text for more information).

At the outcrop scale, the different orientations of the soaked hydrocarbon or carbonate-filled fracture sets measured at the three working sites Kabyosi, SRC, and BAB form "x-crossing" structural pattern, reflecting the local macroscale fault intersections.

Intersection lines of "x-shaped" fault and fracture sets produce dilatational zones under various tectonic stress regimes and provide lateral and vertical optimal channels for fluid flow (e.g., [11, 43–45]). Such structural intersections represent thus "pipe-like" structures that can act as fluid preferential pathways and may be kept open even in compressional stress field [46]. Therefore, the current and fossil fluid outflows at the different working sites highlight that this local "x-crossing" structural pattern produces sufficient relative vertical fracture permeability to drive significant amount of fluids, in regard to other locations along the TBFS without structural intersection.

6.1.3. The Relay Zone of Kabyosi. The Kabyosi hydrocarbon seeps are located at the intersection of ENE-trending faults, parallel to that of the main Kaiso transfer structure, and of secondary NNW- to NNE-trending structural lineaments (Figure 8(a)). Lastly, the SRC site is located at the southern termination of the NE-trending Toro-Bunyoro fault, where it splits into shorter subparallel segments and intersects the ENE-trending Kaiso transfer zone (Figure 3(d)). This geometry could be related to a relay ramp structure with the NE-trending faults, the main faults, and the ENE-trending faults that breach between both the main faults. Fractures, in this relay structure, increase in intensity, and the great

Table 2: Oxygen and carbon isotopic data ($\delta^{18}O_{cc}$ and $\delta^{13}C_{cc}$, ‰) of the analyzed carbonate veins. Oxygen isotopic ratio $\delta^{18}O_{H2O}$ of the carbonate vein source fluids is calculated using Zheng (1999) formula (see text for more information).

Sample	Number of grains analyzed	# of grain	Measurements	$\delta^{13}C_{cc}$ (‰ PDB) average per grain	$\delta^{18}O_{cc}$ (‰SMOW) average per grain	$\delta^{18}O_{H2O}$ (‰ SMOW) average per grain
ug13.33b	13	1	1	6.12	24.08	0.86
		2	1	5.26	22.92	−0.27
		3	1	6.88	30.24	6.88
		4	1	4.15	26.63	3.35
		5	1	3.57	26.81	3.53
		6	1	−0.15	29.33	6.00
		7	1	−3.25	29.69	6.35
		8	1	−5.17	25.88	2.62
		9	2	1.13	25.97	2.71
		10	2	3.18	26.30	3.03
		11	3	−1.01	28.87	5.54
		12	3	1.36	23.46	0.26
		13	3	−1.37	27.97	4.67
ug13.16c	4	1	2	2.57	13.48	−9.50
		2	4	6.35	15.07	−7.94
		3	2	14.78	20.68	−2.46
		4	4	11.84	15.12	−7.89
ug13.44a primary subhedral grains	4	1	6	1.00	16.07	−6.97
		2	3	1.16	19.59	−3.52
		3	8	6.97	17.94	−5.14
		4	1	8.12	17.15	−5.91
ug13.44a secondary anhedral grains	5	1	2	0.75	20.88	−2.26
		2	2	−0.45	23.57	0.36
		3	2	2.68	20.08	−3.05
		4	3	1.64	24.34	1.12
		5	2	1.53	21.30	−1.85

range of orientation leads to a high permeability zone. Following the model proposed by Fossen and Rotevatn [47], this relay ramp locates a fluid flow pattern oriented vertically and parallel to the main fault structure composed by the dense fracture network and reinforced by the impermeable sail formed by the TBFS fault core. It is able to focus fluids coming from the basin.

Consequently, this rift-bounding fault system corresponds to a discontinuous barrier for fluids, with local pathways for transfers from the rift shoulder toward the basin, and vice versa. Relative to barrier parts where fluid pressure may accumulate, local structural intersections and associated "x-crossing" fracture networks therefore represent hydraulically active shear fractures in relatively low compressive stress areas along-strike the normal faults and low fluid pressure areas. Consequently, such areas can either act in the hydrogeological system as discharging zones for connected overpressured fluids (cf. Kabyosi) or as favorable down- and upflow zones that may favor subsurface convection cell development (cf. Kibiro).

Outflows occurring predominantly at the interaction zone and intersection of multiple faults have been described for different fault-controlled geothermal systems in the world (e.g., [18, 48, 49]). A number of studies performed in the Great Basin region (USA) highlighted by an inventory over 400 geothermal active sites that more than half of the sites are hosted by fault interaction features, as step-overs or relay ramps, and fault intersections [19, 20, 50, 51]. Further, the exclusive location of these fluid circulation zones at fault intersections between the TBFS and subsidiary oblique structures suggests that outflow does not significantly occur along the major fault scarp without such a structural interaction. This agrees with the rare occurrence in the Great Basin of geothermal systems along planar midsegments of major faults where displacement generally peaks [19, 20]. Fault intersections and the relay ramp therefore appear as reliable prime targets for exploration, especially as geothermal resources may have little or no surface manifestation (e.g., [15–17]). As part of a petroleum system, the identification of such structural intersections is also critical, as they can represent either reservoir charging or leakage pathways (e.g., [52]).

6.2. A Complex Fluid Mixing Zone. This study and previous investigations allowed to identify three main fluid reservoirs for the current and fossil fluids recognized along the TBFS.

The different fluid inputs and their mixing are schematically represented in Figure 12 and discussed below.

6.2.1. The Meteoric Reservoirs. A number of geochemical and geophysical studies of the Kibiro geothermal prospect area showed that the main recharging fluid of this current system corresponds to meteoric water infiltrated along faults in the eastern rift basement shoulder, along which it percolated underground up to the intersection with the TBFS [22]. Similar results were obtained with this study from oxygen isotopic composition analysis of carbonate veins at sites NRC and BAB (cf. ug13.16 and ug14.44 samples). With both sites located also at the intersection between the TBFS and subsidiary oblique faults, source fluid of these veins also appears to have been infiltrated underground through the faulted basement rift shoulder (Figure 12). The standard fresh surface water values is assumed at -8 ± 7‰ SMOW [53]. This meteoric fluid contribution therefore represents the "external basin fluids" input of the fluid circulations within the TBFS.

6.2.2. The Basin Reservoirs. Hydrocarbon material was sampled from the soaked fractures of the faulted basement footwall in both Kibiro and Kabyosi sites. Due to severe biodegradation of the organic material, their source could not be determined. However, regarding the sampling location along Lake Albert and the proven oil resources in this basin (e.g., [27]), these seepages are assumed to be driven from the petroleum system of the lake. The contribution of basin water is also supported by some relatively high $\delta^{13}C$ values (>6‰ PDB) of carbonate veins measured at sites NRC, BAB, and SRC, where no organic material has been recognized nearby. These unusual values suggest that carbonate source has been partly affected by bacterial methanogenic processes [54–56]. Such isotopic signature could be derived from fluids affected by organic-related processes of the basin sedimentary deposits. Furthermore, Lake Albert water samples show average $\delta^{18}O$ composition of 5.23‰ SMOW ([22]) clearly resulting from an interaction between lake's sediments and meteoric and connate waters [57, 58]. Thus, these lake-related fluids reflect the "internal basin fluid" input of the fluid circulations within the TBFS (Figure 12).

6.2.3. The Deep Reservoirs. Fluid source of the K-feldspar veins identified at NRC, BAB, and SRC, as well as that of the carbonate veins from SRC (cf. ug13.36 sample), is less clear. Adularia is a rather common K-feldspar polymorph, whose mineralization is generally associated to low-temperature hydrothermalism and host-rock alteration in active rifts [59, 60]. The K-feldspar veins observed in this study are therefore considered here as adularia veins. Except being emplaced prior to the carbonate veins, no clear relative timing relationship of these adularia veins during rift evolution could be determined. A number of highly deformed adularia veins are recognized in fault core cataclasis samples from the SRC site, while those from the NRC site look undeformed. Assuming these fault core rocks to be developed during rift-related paroxysmal deformation events, the different adularia veins would have crystallized during rather early stages of the rifting.

6.2.4. Mixing of the Fluids and Transfer. Later carbonate veins observed at site SRC appear different from those characterized at both NRC and BAB sites and those described in the Kibiro geothermal prospect area. Calculated oxygen isotope ratios of fluid source from these veins generally show positive values up to 6.88‰ SMOW (average 3.5‰ SMOW), significantly different from standard fresh surface water values (-8 ± 7‰ SMOW) [53] and Kibiro hot spring water samples (−2.05‰ SMOW) [22]. Such data suggest that meteoric water is clearly not the fluid source for the SRC site carbonate veins. Lake Albert water samples show average $\delta^{18}O$ composition of (5.23‰ SMOW [22]). With similar positive values, the fluid source $\delta^{18}O$ composition of the SRC site carbonate veins is then compatible either with a lake-water origin or with a formation water origin [57, 58], which could both support the "internal basin fluid" input in the hydrogeological TBFS.

The positive $\delta^{18}O$ values from sample ug13.33 are however also compatible with oxygen isotopic composition of deep-seated metamorphic or magmatic fluids [61]. Despite such fluids were not clearly recognized in this study, several arguments support the hypothesis that deep-seated fluids flow up to the TBFS scarp. The strontium isotope analyses of sulfates precipitated at Kibiro indicate an interaction with crustal materials [22]. Evidences of deep circulation of fluids are recognized southwestward along major faults of the ARS basin. The Buranga hydrothermal system, located along the Rwenzori Mountains at about 150 km southwest from Kibiro, is one other major geothermal prospect of the ARS. Meteoric water from the adjacent Rwenzori high ground is recognized as the main recharging fluid of the system but a magmatic gas input, associated to an underlying magmatic heat source, is also strongly suggested by geochemical analyses [22, 62, 63]. Furthermore, a microseismic monitoring campaign of the Rwenzori area showed several earthquake (EQ) clusters between 5 to 16 km deep, localized in the prolongation of the TBFS at about 100–150 km from our study area [64]. From EQ parameters and cluster shape, these authors suggest that these EQ swarms are triggered by deep crustal fluid and gas migration, rising from a postulated magmatic body in the upper mantle. From these arguments, a deep-seated source fluid contribution is therefore considered in the hydrogeological TBFS (Figure 12). Fluid flow along the deeply rooted crustal-scale ARS-bounding faults may contribute to the circulations that formed some of the identified adularia and carbonate veins, as well as other potential mineral phases unseen during this study.

Information from the fluid circulation investigations along the TBFS indicates therefore that this rift-bounding structure is connected to three sorts of fluid reservoirs providing "external basin fluids" (i.e., meteoric waters), "internal basin fluids" (i.e., HC and sediment formation waters), and deep-seated crustal fluids (i.e., magmatic or deep down flowing meteoric fluids) (Figure 12). The fault core of the TBFS contributes to a compartmentalization of the hydrogeological system, but the other elements of the

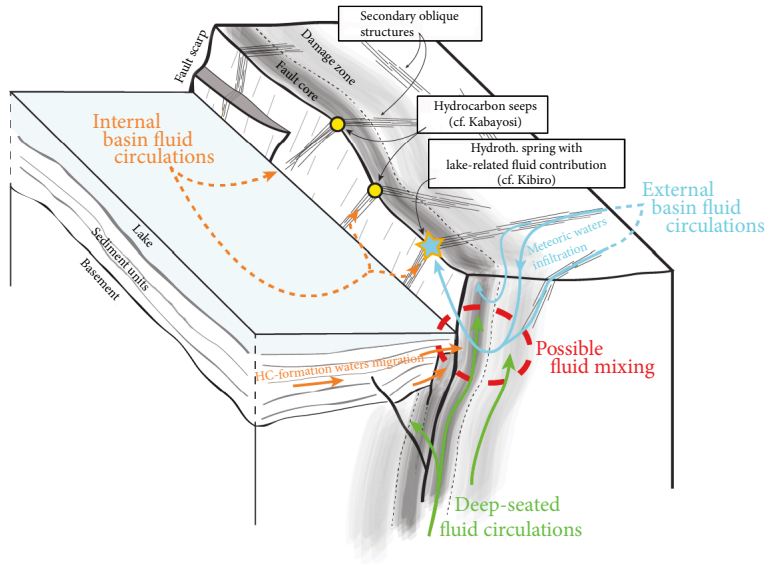

Figure 12: Schematic 3D bloc model of a rift-bounding fault system illustrating the three fluid inputs that flow and mix into the damage zone and fault core compartments (see text for more information). Oblique preexisting reactivated faults or new rift-related conjugated faults can drive fluids in the hydrogeological system. Structural intersections with the main fault system represent preferential discharging zone for subsurface fluids.

hydrogeological system contribute to interrupt and pass through the barrier. The damage zones of the TBFS, the deeply rooted major structure, are able to flow up deep fluids. The relay zone and the oblique structures are the main pathway to transport basin fluids, including hydrocarbons, toward the rift shoulders and through the TBFS fault core. The dense fracture network developed in the rift shoulder is the preferential pathway to flow down the meteoric fluids toward the deep part of the rift especially through the "x-crossing" fracture.

All these features form a composite hydrogeological system, where fluids circulate within the highly fractured fault compartments and converge preferentially up to the surface along relatively low-stress zones formed by structural intersections between the TBFS and subsidiary oblique structures. Through the "x-crossing" fracture networks associated to these intersections, fluid inputs can flow and mix across the fracture porosity of the fault system damage zones.

7. Conclusion

This study documents the complexity of a hydrogeological system hosted by a major rift-bounding fault system and suggests that a number of internal- and external-rift basin fluids can supply it over time. Structural and petrological data gathered along the TBFS emphasize the role of local structural intersections with subsidiary oblique structures for fluid flow. It therefore contributes to the recognition of generic favorable structural settings of fault-controlled geothermal systems or hydrocarbon storage. With fault intersections providing local relatively permeable and low-stress areas, the rift-bounding fault system represents a discontinuous barrier for fluids where structural intersections control preferential outflow zones and channel fluid transfers from the rift shoulder to the basin, and vice versa. Inputs from 3 types of fluid reservoirs are recognized within this fault-hosted hydrogeological system, with "external basin fluids" (i.e., meteoric waters), "internal basin fluids" (i.e., hydrocarbons and sediment formation waters), and deep-seated crustal fluids (i.e., magmatic fluids) (Figure 12). Such a major rift-bounding fault system finally represents a composite hydrogeological system in which significant economic amounts of fluids preferentially converge and show surface manifestations locally at structural intersections. Fault intersections therefore appear as reliable prime targets for exploration of fault-controlled geothermal systems.

Data Availability

Samples and datasets used and produced during this study are all available at the GeoRessources Lab (University of Lorraine, France).

Conflicts of Interest

The authors declare that they have no conflicts of interest.

Acknowledgments

This work was supported by a PhD grant from Total and GeoRessources Lab.

References

[1] R. Bertani, "Geothermal power generation in the world 2010–2014 update report," *Geothermics*, vol. 60, pp. 31–43, 2016.

[2] K. C. Lee, "Classification of geothermal resources by exergy," *Geothermics*, vol. 30, no. 4, pp. 431–442, 2001.

[3] J. W. Lund and T. L. Boyd, "Direct utilization of geothermal energy 2015 worldwide review," *Geothermics*, vol. 60, pp. 66–93, 2016.

[4] P. Muffler and R. Cataldi, "Methods for regional assessment of geothermal resources," *Geothermics*, vol. 7, no. 2-4, pp. 53–89, 1978.

[5] S. K. Sanyal, "Classification of geothermal systems–a possible scheme," in *Thirtieth Workshop on Geothermal Reservoir Engineering*, pp. 85–88, Stanford University, Stanford, CA, USA, 2005.

[6] C. F. Williams, M. J. Reed, and A. F. Anderson, "Updating the classification of geothermal resources," in *Proceedings, Thirty-Sixth Workshop on Geothermal Reservoir Engineering*, Stanford, CA, USA, 2011.

[7] M. Wilmarth and J. Stimac, "Power density in geothermal fields," in *Proceedings World Geothermal Congress 2015*, p. 7, Melbourne, Australia, 2015.

[8] J. Limberger, P. Calcagno, A. Manzella et al., "Assessing the prospective resource base for enhanced geothermal systems in Europe," *Geothermal Energy Science*, vol. 2, no. 1, pp. 55–71, 2014.

[9] I. S. Moeck, "Catalog of geothermal play types based on geologic controls," *Renewable and Sustainable Energy Reviews*, vol. 37, pp. 867–882, 2014.

[10] D. Mckenzie, "Some remarks on the development of sedimentary basins," *Earth and Planetary Science Letters*, vol. 40, no. 1, pp. 25–32, 1978.

[11] R. H. Sibson, "Fluid involvement in normal faulting," *Journal of Geodynamics*, vol. 29, no. 3-5, pp. 469–499, 2000.

[12] C. J. Ebinger, "Tectonic development of the western branch of the East African rift system," *Geological Society of America Bulletin*, vol. 101, no. 7, pp. 885–903, 1989.

[13] J. E. Faulds, N. Hinz, C. Kreemer, and M. Coolbaugh, "Regional patterns of geothermal activity in the Great Basin region, Western USA: correlation with strain rates," *Geothermal Resources Council Transactions*, vol. 36, pp. 897–902, 2012.

[14] A. Genter, L. Guillou-Frottier, J.-L. Feybesse, N. Nicol, C. Dezayes, and S. Schwartz, "Typology of potential hot fractured rock resources in Europe," *Geothermics*, vol. 32, no. 4-6, pp. 701–710, 2003.

[15] M. F. Coolbaugh, G. L. Raines, R. E. Zehner, L. Shevenell, and C. F. Williams, "Prediction and discovery of new geothermal resources in the Great Basin: multiple evidence of a large undiscovered resource base," *Geothermal Resources Council Transactions*, vol. 30, pp. 867–873, 2006.

[16] M. C. Hanson, C. Oze, and T. W. Horton, "Identifying blind geothermal systems with soil CO_2 surveys," *Applied Geochemistry*, vol. 50, pp. 106–114, 2014.

[17] M. Person, S. Kelley, R. Kelley et al., "Hydrogeologic windows: detection of blind and traditional geothermal play fairways in southwestern New Mexico using conservative element concentrations and advective-diffusive solute transport," *Geothermal Resources Council Transactions*, vol. 39, pp. 751–759, 2015.

[18] D. Curewitz and J. A. Karson, "Structural settings of hydrothermal outflow: fracture permeability maintained by fault propagation and interaction," *Journal of Volcanology and Geothermal Research*, vol. 79, no. 3-4, pp. 149–168, 1997.

[19] J. E. Faulds and N. H. Hinz, "Favorable tectonic and structural settings of geothermal systems in the Great Basin region, Western USA: proxies for discovering blind geothermal systems," in *Proceedings World Geothermal Congress 2015*, p. 6, Melbourne, Australia, 2015.

[20] J. E. Faulds, N. H. Hinz, M. F. Coolbaugh et al., "Assessment of favorable structural settings of geothermal systems in the Great Basin, Western USA," *GRC Transactions*, vol. 35, pp. 777–783, 2011.

[21] N. H. Hinz, M. Coolbaugh, L. Shevenell, P. Stelling, G. Melosh, and W. Cumming, "Favorable structural – tectonic settings and characteristics of globally productive arcs," in *41st Workshop on Geothermal Reservoir Engineering*, Stanford University, Stanford, CA, USA, 2016.

[22] G. Bahati, Z. Pang, H. Ármannsson, E. M. Isabirye, and V. Kato, "Hydrology and reservoir characteristics of three geothermal systems in western Uganda," *Geothermics*, vol. 34, no. 5, pp. 568–591, 2005.

[23] K. Aanyu and D. Koehn, "Influence of pre-existing fabrics on fault kinematics and rift geometry of interacting segments: analogue models based on the Albertine Rift (Uganda), western branch-East African Rift system," *Journal of African Earth Sciences*, vol. 59, no. 2-3, pp. 168–184, 2011.

[24] A. B. Katumwehe, M. G. Abdelsalam, and E. A. Atekwana, "The role of pre-existing Precambrian structures in rift evolution: the Albertine and Rhino grabens, Uganda," *Tectonophysics*, vol. 646, pp. 117–129, 2015.

[25] C. K. Morley, *Geoscience of Rift Systems: Evolution of East Africa*, AAPG studies in geology. American Association of Petroleum Geologists, Tulsa, Okla, 1999.

[26] D. Abeinomugisha and R. Kasande, "Tectonic control on hydrocarbon accumulation in the intracontinental Albertine Graben of the East African Rift system," *Tectonics and Sedimentation*, vol. 100, pp. 209–228, 2013.

[27] D. Lirong, W. Jianjun, C. Dingsheng et al., "Geological conditions and petroleum exploration potential of the Albertine Graben of Uganda," *Acta Geologica Sinica - English Edition*, vol. 78, no. 4, pp. 1002–1010, 2004.

[28] T. Karp, C. A. Scholz, and M. M. McGlue, "Structure and stratigraphy of the Lake Albert Rift, East Africa; observations from seismic reflection and gravity data," *AAPG Memoir*, vol. 95, pp. 299–318, 2012.

[29] P. Virransalo, P. Härmä, J. Pokki, T. Manninen, M. Lehtonen, and T. Koistinen, *Geological Map of Uganda, Hoima, Sheet N° NA-36-9., Scale 1/250000*, GTK Consortium, 2012.

[30] A. B. P. Westerhof, P. Härmä, E. M. Isabirye et al., *Geology and Geodynamic Development of Uganda with Explanation of the 1:1,000,000-Scale Geological Map, Special Paper /Geological Survey of Finland*, Geological Survey of Finland, Espoo, Finland, 2014.

[31] K. Link, D. Koehn, M. G. Barth et al., "Continuous cratonic crust between the Congo and Tanzania blocks in western Uganda," *International Journal of Earth Sciences*, vol. 99, no. 7, pp. 1559–1573, 2010.

[32] C. Rollion-Bard, D. Mangin, and M. Champenois, "Development and application of oxygen and carbon isotopic measurements of biogenic carbonates by ion microprobe," *Geostandards and Geoanalytical Research*, vol. 31, no. 1, pp. 39–50, 2007.

[33] K. B. Alexander, W. Cumming, and L. Marini, "Technical review of geothermal potential of Kibiro geothermal prospect, Uganda," in *Proceedings of the 6th African Rift Geothermal Conference*, Addis Ababa, Ethiopia, 2016.

[34] P. Mawejje, V. Kato, J. Nnakirijja et al., "The geology and potential of Kibiro geothermal field in Albertine Graben, western Uganda," *Proceedings of the World Geothermal Congress*, 2015, pp. 1–11, Melbourne, Australia, 2015.

[35] I. Tumwikirize, "Thoughts about techniques applicable in exploration of geothermal resources in Uganda," in *Proceedings of the Third East African Rift Geothermal Conference*, pp. 121–138, Djibouti, Djibouti, 2010.

[36] G. Bahati, K. Vincent, and N. Catherine, "Geochemistry of Katwe-Kikorongo, Buranga and Kibiro geothermal areas, Uganda," in *Proceedings of the Third East African Rift Geothermal Conference*, pp. 223–230, Djibouti, Djibouti, 2010.

[37] J. F. Natukunda, "Geology of Kibiro, Katwe and Buranga geothermal prospects of Uganda," in *Proceedings of the World Geothermal Congress*, pp. 1–13, Bali, Indonesia, 2010.

[38] H. Ármannsson, *Geochemical Studies on Three Geothermal Areas in West and Southwest, Uganda. Final Report*, Geothermal Exploration UGA/92/003, UNDESD, GSMD, Uganda, 1994.

[39] D. K. Muhwezi, "The potential relationship of some geothermal field in Uganda," in *Proceedings of the Third East African Rift Geothermal Conference*, pp. 365–382, Djibouti, Djibouti, 2010.

[40] V. F. Bense, T. Gleeson, S. E. Loveless, O. Bour, and J. Scibek, "Fault zone hydrogeology," *Earth-Science Reviews*, vol. 127, pp. 171–192, 2013.

[41] J. S. Caine, J. P. Evans, and C. B. Forster, "Fault zone architecture and permeability structure," *Geology*, vol. 24, no. 11, pp. 1025–1028, 1996.

[42] D. R. Faulkner, C. A. L. Jackson, R. J. Lunn et al., "A review of recent developments concerning the structure, mechanics and fluid flow properties of fault zones," *Journal of Structural Geology*, vol. 32, no. 11, pp. 1557–1575, 2010.

[43] D. A. Ferrill, A. P. Morris, and R. N. McGinnis, "Crossing conjugate normal faults in field exposures and seismic data," *AAPG Bulletin*, vol. 93, no. 11, pp. 1471–1488, 2009.

[44] M. Person, A. Hofstra, D. Sweetkind et al., "Analytical and numerical models of hydrothermal fluid flow at fault intersections," *Geofluids*, vol. 12, no. 4, pp. 312–326, 2012.

[45] R. H. Sibson, "Structural permeability of fluid-driven fault-fracture meshes," *Journal of Structural Geology*, vol. 18, no. 8, pp. 1031–1042, 1996.

[46] I. S. Moeck, S. Uhlig, B. Loske, A. Jentsch, R. F. Mählmann, and S. Hild, "Fossil multiphase normal faults - prime targets for geothermal drilling in the Bavarian Molasse Basin?," in *Proceedings World Geothermal Congress 2015*, p. 7, Melbourne, Australia, 2015.

[47] H. Fossen and A. Rotevatn, "Fault linkage and relay structures in extensional settings-a review," *Earth-Science Reviews*, vol. 154, pp. 14–28, 2016.

[48] J. V. Rowland and R. H. Sibson, "Structural controls on hydrothermal flow in a segmented rift system, Taupo Volcanic Zone, New Zealand," *Geofluids*, vol. 4, no. 4, pp. 259–283, 2004.

[49] A. Taillefer, R. Soliva, L. Guillou-Frottier, E. Le Goff, G. Martin, and M. Seranne, "Fault-related controls on upward hydrothermal flow: an integrated geological study of the Têt Fault System, Eastern Pyrénées (France)," *Geofluids*, vol. 2017, pp. 1–19, 2017.

[50] N. H. Hinz, M. F. Coolbaugh, J. E. Faulds, D. L. Siler, and G. Dering, "Building the next generation of regional geothermal potential maps: examples from the Great Basin region, Western USA," in *Proceedings World Geothermal Congress 2015*, p. 12, Melbourne, Australia, 2015.

[51] D. L. Siler, J. E. Faulds, B. Mayhew, and D. D. McNamara, "Analysis of the favorability for geothermal fluid flow in 3D: Astor Pass geothermal prospect, Great Basin, northwestern Nevada, USA," *Geothermics*, vol. 60, pp. 1–12, 2016.

[52] A. Gartrell, Y. Zhang, M. Lisk, and D. Dewhurst, "Fault intersections as critical hydrocarbon leakage zones: integrated field study and numerical modelling of an example from the Timor Sea, Australia," *Marine and Petroleum Geology*, vol. 21, no. 9, pp. 1165–1179, 2004.

[53] R. E. Criss, *Principles of Stable Isotope Distribution*, Oxford University Press, New York, NY, USA, 1999.

[54] J. M. Budai, A. M. Martini, L. M. Walter, and T. C. W. Ku, "Fracture-fill calcite as a record of microbial methanogenesis and fluid migration: a case study from the Devonian Antrim Shale, Michigan Basin," *Geofluids*, vol. 2, no. 3, pp. 162–183, 2002.

[55] C. D. Curtis, M. L. Coleman, and L. G. Love, "Pore water evolution during sediment burial from isotopic and mineral chemistry of calcite, dolomite and siderite concretions," *Geochimica et Cosmochimica Acta*, vol. 50, no. 10, pp. 2321–2334, 1986.

[56] J. Hoefs, *Stable Isotope Geochemistry*, Springer Berlin Heidelberg, Berlin, Heidelberg, 2009.

[57] F. J. Longstaffe, "Stable isotope studies of diagenetic processes," in *Stable Isotope Geochemistry of Low Temperature Processes, Short Course Handbook*, T. K. Kyser and R. Kerrich, Eds., p. 452, Mineralogical Association of Canada, Saskatoon, Saskatchewan, 1987.

[58] Z. Sharp, *Principles of Stable Isotope Geochemistry*, Pearson/-Prentice Hall, Upper Saddle River, NJ, USA, 1st edition, 2007.

[59] P. Černy and R. Chapman, "Adularia from hydrothermal vein deposits; extremes in structural state," *Canadian Mineralogist*, vol. 24, pp. 717–728, 1986.

[60] G. Dong and G. W. Morrison, "Adularia in epithermal veins, Queensland: morphology, structural state and origin," *Mineralium Deposita*, vol. 30, no. 1, pp. 11–19, 1995.

[61] H. L. Barnes, Ed., *Geochemistry of Hydrothermal Ore Deposits*, Wiley, New York, NY, USA, 3rd edition, 1997.

[62] V. Kato and M. Kraml, "Geochemistry of Rwenzori hot spring waters," in *Proceedings of the 3rd East African Rift Geothermal Conference*, p. 12, Djibouti, Djibouti, 2010.

[63] J. F. Natukunda and G. Bahati, "Status of geothermal energy exploration at Buranga prospect western Uganda," in *Proceedings of the 6th African Rift Geothermal Conference*, p. 13, Addis Ababa, Ethiopia, 2016.

[64] M. Lindenfeld, G. Rümpker, K. Link, D. Koehn, and A. Batte, "Fluid-triggered earthquake swarms in the Rwenzori region, East African Rift—evidence for rift initiation," *Tectonophysics*, vol. 566-567, pp. 95–104, 2012.